BIOLOGICALLY TRIGGERED NANO-FORMULATIONS FOR PREVENTION AND TARGETING OF BACTERIAL BIOFILM

Daniyar Yestay

Submitted to the Department of Chemical and Materials Engineering in partial of the requirements for the degree of a Master of Science in Biomedical Engineering

School of Engineering and Digital Sciences

Department of Chemical and Materials Engineering

Nazarbayev University

Supervisors:

Lead Supervisor Name: Professor Vesselin Paunov

Co-supervisor Name: Professor Amro Khalil

Co-supervisor Name: Professor Cevat Erisken

April 2025

Abstract

The research thesis develops and characterizes biologically triggered nano-formulations along with their testing process for bacterial biofilms prevention and targeting. The production of biofilm communities of bacteria through a self-made extracellular polymer substance makes these microbial groups highly resistant to common antibiotics and results in serious treatment barriers during medical care, particularly for persistent infections. The main goal of this study was to develop and analyze novel nanomaterials that would provide controlled tetracycline hydrochloride drug release to combat bacterial biofilm resistance factors. The nano-formulation is based on polyacrylic acid nanogel (Carbopol Aqua SF1) as its core, which is loaded with tetracycline and then coated with a subsequent layers of bovine serum albumin (BSA) and Shellac. This coating creates a protective shell, encapsulating the antibiotic in the core but contains weak portion inclusions to enable bacterial protease-triggered drug release specifically within biofilm environments. In vitro and in vivo studies demonstrated that this nano-formulated antibiotic delivery system succeeded in both blocking biofilm formation and slowing down bacterial development with low toxicity effects on human keratinocyte cells. This research findings indicate that the antibiotic-loaded BSA-shellac coated Carbopol formulation serves as a promising prevention agent for biofilm-based bacterial infections as it offers controlled drug and biological stimuli responsive delivery system for controlled drug release.

Acknowledgments

I want to thank all the people who guided and assisted me during the thesis writing process.

First, I extend my sincere thanks to my supervisor, Prof. Vesselin Paunov, for his outstanding supervision, which guided me, shaping this project through his advice and constant review. Through his expertise and support, he has significantly contributed to my academic and personal development.

This research was notably improved through the valuable feedback received from Prof. Amro Khalil and Prof. Cevat Erisken, who served as my thesis co-supervisors.

The colleagues and friends at the Advanced Biomedical Nanotechnology Laboratory deserve my gratitude, as they provided continuous support through discussions and personal motivation during the entire research process. Participating in the lab's academic environment provided both intellectual enrichment and personal throughout this experience.

This research benefited greatly from the technical assistance of Nurgul Daniyeva and Alisher Rapikov, who serve as Research Technologists at Nazarbayev University, for their work with TEM and SEM imaging. The successful completion of this research depended on their specialized knowledge and experience.

The boundless love, patience, and continuous support of my parents have been the foundation of my gratitude toward them.

The resources and financial support for this research project were provided by Nazarbayev University.

I express my gratitude to everyone who made this project possible.

Table of Contents

Abstract 2

List of Figures 6

List of Tables 8

List of Abbreviations 9

Introduction 11

1.1 Bacterial Biofilm 11

1.2 Biofilm-Associated Infections 12

1.3 Nanotechnology in Biofilm Treatment 16

1.4 Research Gaps and Objectives 18

Materials and methods 20

2.1 Materials and Methods 20

2.2 Preparation of Nanoformulations loaded with Tetracycline Hydrochloride 21

2.3 Characterization of the Nanoformulations 23

2.4 In Vitro Enzyme-Triggered Drug Release 24

2.5 In Vivo Bacteria Triggered Drug Release 25

2.6 Cytotoxicity on Human Keratinocytes 27

2.7 Statistical Analysis 28

Results and Discussion 29

3.1 Characterization of Nano-formulations 30

3.2 Preparation of Tetracycline Hydrochloride loaded Nano-formulations 41

3.3 In Vitro Enzyme-Triggered Drug Release 43

3.4 In Vivo Bacteria Triggered Drug Release 45

3.5 Cytotoxicity 54

Conclusion 58

Bibliography 60

List of Figures

Figure 2.2. 1: Schematic representation of the loading and coating process for Carbopol Aqua SF1 nanogels with tetracycline hydrochloride (TC-HCL), BSA, and shellac ammonium salt. The process includes pH adjustments at different stages to facilitate swell 22

Figure 3.1. 1: Average hydrodynamic diameter and zeta potential distribution of Carbopol Aqua SF1 nanogel in different pH levels. 32

Figure 3.1. 2: Average hydrodynamic diameter and zeta potential distribution of BSA in different pH levels. 34

Figure 3.1. 3: Average hydrodynamic diameter and zeta potential distribution of shellac in different pH levels. 35

Figure 3.1. 4: ATR-FTIR Spectroscopy of Individual Components and Formulation..... 38

Figure 3.1. 5: Morphological imaging of BSA and shellac coated Carbopol particles. Representative TEM image of a sample of (A) Carbopol only, (B) BSA only, (C) BSA coated Carbopol, and (D,E) shellac/BSA coated Carbopol. 39

Figure 3.1. 6: SEM Imaging of (A) Carbopol and (B) BSA-Shellac-Coated Carbopol Particles. ... 40

Figure 3.2. 1: Hydrodynamic Diameter of Drug-Loaded Carbopol, BSA-Coated Carbopol, and BSA-Shellac Coated Carbopol Nanoparticles at pH 3.33. 42

Figure 3.2. 2: Zeta potential of Drug-Loaded Carbopol, BSA-Coated Carbopol, and BSA-Shellac Coated Carbopol Nanoparticles at pH 3.33. 43

Figure 3.3. 1: Tetracycline release kinetic curve of the (i) non coated loaded Carbopol, (ii) BSA/shellac coated TC loaded Carbopol and (iii) the BSA/shellac coated TC loaded Carbopol in the presence of 1 wt% trypsin over the course of 41 hours. 45

Figure 3.4. 1: Percentage of residual bacterial biofilm from S. epidermidis following 24h of growth under a variety of treatments with different air-dried aliquots of air dried non-loaded coated Carbopol, loaded non-coated Carbopol and loaded coated with BSA/shellac. 47

Figure 3.4. 2: CFU counts per mL of the PBS extract from the residual biofilm to account for the viable bacteria (S. epidermidis) following 24h of build up of a biofilm from bacterial broth in the presence of a variety of treatments at different aliquots of air-dried formulations compared with the control (no treatment). 49

Figure 3.4. 3: Percentage of residual bacterial biofilm from S. epidermidis following 24h of growth under a variety of treatments with different aliquots non-loaded coated Carbopol, loaded non-coated Carbopol and loaded coated with BSA/shellac mixed with bacterial broth. 51

Figure 3.4. 4: CFU counts per mL of the PBS extract from the residual biofilm to account for the viable bacteria (S. epidermidis) following 24h of build up of a biofilm from bacterial broth in the presence of a variety of treatments at different aliquots and compared with the control (no treatment). 53

Figure 3.5. 1: Cell Proliferation of Drug-Loaded and Unloaded Formulations. Cell proliferation was assessed by measuring the percentage of cell growth following treatment with drug-loaded and drug-unloaded formulations at various concentrations (10 μL, 20 μL, and 30 μL) 55

Figure 3.5. 2: Cell Viability of Drug-Loaded and Unloaded Formulations. Cell viability was measured using the viability assay for drug-loaded and drug-unloaded formulations at different concentrations (10 μL, 20 μL, and 30 μL)..... 56

List of Tables

Table 1.2. 1: Medical devices and their associated common pathogens. 13

List of Abbreviations

AgNPs	Silver nanoparticles
ATR-FTIR	Attenuated Total Reflectance Fourier Transform Infrared Spectroscopy
AuNPs	Gold nanoparticles
BSA	Bovine Serum Albumin
CAUTI	Catheter-associated urinary tract infections
CFU	Colony Forming Unit
CRS	Chronic rhinosinusitis
CV	Crystal Violet
DLS	Dynamic Light Scattering
DMEM	Dulbecco's Modified Eagle Medium
ELS	Electrophoretic Light Scattering
EPS	Extracellular Polymeric Substances
eDNA	Extracellular DNA
FBS	Fetal Bovine Serum
HBSS	Hanks' Balanced Salt Solution
HGT	Horizontal gene transfer
MBC	Minimum Bactericidal Concentration
MIC	Minimum Inhibitory Concentration
NPs	Nanoparticles
O/N	Overnight
PBS	Phosphate-Buffered Saline

pH	Potential of Hydrogen
PMNs	Polymorphonuclear leukocytes
ROS	Reactive oxygen species
rpm	Revolutions per minute
SEM	Scanning Electron Microscopy
TC-HCL	Tetracycline hydrochloride
TEM	Transmission Electron Microscopy
UV-Vis	Ultraviolet–Visible
ZnO NPs	Zinc Oxide nanoparticles

Chapter 1

Introduction

1.1 Bacterial Biofilm

Bacterial biofilms are a community of microorganisms that form on the surfaces of implants and biomedical devices, as well as in internal or chronic wounds. They can be multi-strain or single-species of microorganisms that live within a self-produced matrix of extracellular polymeric substances (EPS). It consists of a complex mixture of glycoproteins, polysaccharides, lipids, and extracellular DNA (eDNA) [1][2]. The protective features of the EPS help biofilms resist multiple forms of environmental stressors and chemicals as well as providing resistance to antimicrobial treatments. In contrast to the planktonic form of the same strain, the bacteria within the biofilm are more resistant due to the processes of antibiotic absorption, deactivation, neutralization, and destruction by the extracellular enzymes of the biofilm and pH [3]. Also, biofilms serve as a source of major chronic infection sites which create adaptive inflammatory reactions. The latter stop the immune system clearance of the biofilms while presenting major problems in chronic wounds, heart valves, lungs, medical implants [4]. As a result, biofilm-associated infections show extreme difficulty in medical management since they resist attack from both immune system defenses and antibiotics.

Bacterial biofilm undergoes of four general steps of development: (i) initial reversible attachment to the colonized surface, (ii) development of a microcolony within a shared EPS, (iii) growth and maturation of the biofilm, (iv) dispersion and release of free-floating cells to colonize new locations [5]. During the first stage of biofilm development, bacteria attach to a surface using non-

specific physical forces such as Van der Waals, electrostatic, and hydrophobic interactions. Further, the secretion of quorum sensing signaling molecules as cyclic dimeric guanosine monophosphate (di-GMP) stimulates EPS production and biofilm maturation. As a result, bacteria produce and secrete an EPS matrix, which is the main component of the bacterial biofilm. Development of EPS and an increase in number, result in the formation of a three-dimensional structure with channels for nutrient and waste exchange. Finally, cyclic dimeric guanosine monophosphate (di-GMP) levels decrease, which promotes the detachment of bacteria. This results in the relocation of bacteria to new surfaces, potentially forming new biofilms [6].

1.2 Biofilm-Associated Infections

According to statistics, around 80% of microbial and chronic infections in the human body are associated with bacterial biofilm formation [7]. The U.S. Centers for Disease Control and Prevention (CDC) reported that pathogenic biofilm infections have caused approximately 23,000 deaths and 3 million infections annually. Predictions suggest that by 2050, antimicrobial-resistant pathogenic biofilms could lead to 300 million premature deaths and cause an economic loss of $100 trillion USD [8].

Bacterial biofilm-related diseases can be broadly divided into two main categories based on the source of infection: device-related and non-device-related infections [9]. Biofilms on medical device surfaces act as the main cause of device-related infections, which allow bacteria to easily colonize the medical device or implant. Microbial infections commonly develop on various medical tools, including central venous catheters, urinary catheters, endoscopes, and mechanical heart valves. Medical devices working in nutrient-rich or humid environments create optimal conditions that drive bacterial colonization and the development of biofilms [10].

One of the most common medical device-related infections is catheter-associated urinary tract infections (CAUTI). Bacteria frequently associated with CAUTI include *Klebsiella pneumoniae*, *Enterococcus* spp., uropathogenic *Escherichia coli* (UPEC), *Pseudomonas aeruginosa*, *Proteus mirabilis*, and others. The process where bacteria create biofilms inside and outside the catheter results in uropathogen entry and bladder persistence. The process of catheter encrustation is mainly influenced by *Proteus mirabilis* and other urease-producing bacteria, which generate calcium and magnesium phosphate precipitates. Biofilms and encrustations act as major contributors that lead to the serious complications and death resulting from CAUTI [11]. Other examples of medical device-related bacterial biofilm infections are presented in Table 1.2.1, with common pathogens that correspond to the specific device.

Table 1.2. 1: Medical devices and their associated common pathogens.

Medical Device	**Common Pathogen**	**References**
Endotracheal tubes	*Enterococcus faecalis, Staphylococcus aureus, Klebsiella pneumoniae, Acinetobacter baumannii, Pseudomonas aeruginosa and Enterobacter spp.*	[12]
Orthopedic devices	*S. aureus*	[13]
Intravascular catheters	*S.aureus,* coagulase-negative staphylococci, *Enterococcus spp, Corynebacterium and Bacillus spp Pseudomonas aeruginosa, Stenotrophomonoas maltophilia and Acinetobacter* species, *Candida sp*	[14]
Contact lenses	*Pseudomonas aeruginosa, Serratia marcescens,*	[15]

	Staphylococcus aureus, Gram-negative bacteria*, Candida albicans*	
Valves, pacemaker, and cardiac medical device	Staphylococci, Streptococci, *Cryptococcus neoformans*	[10]
Respiratory device	*Aspergillus fumigatus* species	[10]
Urinary catheters	*Enterococcus faecalis*	[10]
Cerebrospinal shunts	*Staphylococcus aureus, Propionibacterium*	[10]
Dental implants	*Fusobacterium, Neisseria, Veillonella* and *Prevotella*	[16]
Central venous catheter	*Staphylococcus aureus S. epidermidis, Streptococcus viridans, Enterococcus* spp. *Escherichia coli, Klebsiella pneumoniae, Proteus mirabilis, Enterobacter Pseudomonas aeruginosa, Candida albicans*, and other Coagulase negative staphylococci (CNS)	[17]

In addition to device-related infections, non-device-related biofilm infections also present a major challenge in clinical settings. Bacterial infections that develop on human tissue surfaces transform into long-lasting conditions that resist defensive actions from the host immune system and medical antibiotics. Infections such as periodontal disease, chronic osteomyelitis, and chronic rhinosinusitis (CRS) represent typical cases of such infections. The major bacteria responsible for periodontal disease biofilms consist of *Porphyromonas gingivalis* alongside other microbial species that colonize teeth and gums. The formation of biofilms leads to tissue damage, which ultimately results in permanent tooth loss if medical treatment is not received. Chronic osteomyelitis, a bone

infection typically caused by *Staphylococcus aureus*, forms biofilms on bone tissue that protect bacteria from immune defense and antibiotic treatments. The bacterial infection called chronic rhinosinusitis (CRS) develops when sinus cavity biofilms made from *Streptococcus pneumoniae* and *Staphylococcus aureus* bacteria persist and start causing resistant inflammatory conditions that cannot be treated with standard therapies [9].

The immune system fails to respond effectively against biofilm infections because the biofilm matrix creates protective layers. The biofilm matrix protects bacterial communities from immune cells and antimicrobial agents, which enables infection survival, especially during chronic conditions. When biofilms receive polymorphonuclear leukocytes (PMNs) that attempt to eliminate the bacteria, they cause necrosis in these immune cells and produce extracellular DNA (eDNA). The bacterial eDNA produces a defensive barrier that blocks both immune defenses and antibiotic molecules. For example, biofilms of *Pseudomonas aeruginosa* use eDNA to create physical structures in cystic fibrosis (CF) patients, which reduces the effectiveness of tobramycin antibiotics. Furthermore, biofilm formation stimulates neutrophil extracellular traps (NETs) to restrict bacterial spread and block antibiotics from accessing the biofilm [18].

In addition to these immune evasion strategies, bacteria located within biofilms function as a defense mechanism to enhance their antibiotic resistance through multiple biological mechanisms. For example, bacteria in biofilms can enter inactive states where they become less vulnerable to antibiotics that mainly affect dividing cells. This phenomenon is particularly evident in chronic infections, where biofilm-associated bacteria survive prolonged exposure to antimicrobial agents [18].

Also, the formation of biofilms creates conditions that drive horizontal gene transfer (HGT) between bacteria, causing increased antibiotic resistance to spread. Closely located bacteria in

biofilms have the ability to exchange resistance genes through conjugation, transformation, and transduction mechanisms. Furthermore, biofilms can enhance antibiotic degradation through several mechanisms. The protective extracellular matrix functions as a barrier to antibiotics because it decreases their ability to penetrate the matrix effectively. For example, some antibiotics, particularly positively charged aminoglycosides, interact with eDNA in the matrix, which slows their penetration into the biofilm [18].

Finally, biofilms contain bacterial enzymes that break down antibiotics, making these drugs less impactful for medical treatment. For example, biofilm-based bacteria infections become resistant to β-lactam antibiotics through the bacterial production of β-lactamases enzymes, which destroy the medical properties of the drug. This enzymatic activity is part of the biofilm's defense system, contributing to the overall resistance observed in biofilm - associated infections [18].

1.3 Nanotechnology in Biofilm Treatment

Standard practices that use extended antibiotic treatment or device replacement to address bacterial biofilms generally fail to remove all biofilm infections. Also, standard antimicrobial therapies are unable to effectively combat biofilms because of their high antibiotic resistance, along with the protective biofilm EPS. Surgical removal remains an option; however, it is invasive, carries significant risks, and does not guarantee that the infection will not recur. Therefore, alternative strategies are urgently needed to combat biofilm-associated infections [19].

Scientists use nanotechnology as an effective solution to resolve such challenges. The exceptional physicochemical properties of nanomaterials include enlarged surface-area-to-volume ratios, along with improved permeability capabilities and modification possibilities, which lead to better biofilm and bacterial cell engagement.

Multiple forms of nanomaterials exist as potential treatments for biofilms and their eradication processes. Antibacterial activity against biofilms has been successfully demonstrated by metal-based nanoparticles such as silver (AgNPs), zinc oxide (ZnO NPs), and gold (AuNPs). These nanoparticles achieve their antibacterial effects through reactive oxygen species (ROS) production, which damages membranes and disrupts the matrix structures of biofilms. The antibiofilm properties of silver nanoparticles have become particularly noticeable because these particles can penetrate and embed into the EPS to damage microorganisms both inside and outside the biofilm. However, the cytotoxicity of these particles still requires more research; their surface if functionalization can reduce cytotoxicity [20].

Another attractive alternative strategy is polymeric and lipid-based nanoparticles. The formation of antimicrobial agent-encapsulated nanoparticles from biodegradable materials allows targeted drug delivery within the biofilm microenvironment. This method improves drug penetration capabilities while minimizing exposure to harmful levels in the bloodstream and raising antibiotic concentrations at the infection site. In addition, stimuli-responsive nanocarriers have been developed to release therapeutic agents in response to specific triggers, such as changes in pH, enzymatic activity, or external stimuli like ultrasound. These smart systems ensure that the antimicrobial effect is precisely targeted at the site of infection and the specific biofilm development stage, minimizing collateral damage to healthy tissues [20].

Multiple obstacles exist that prevent nanotechnological approaches from being widely used for biofilm elimination in medical settings. Metal-based nanoparticles, including AgNPs and ZnO NPs, although effective as biofilm preventive agents, encounter issues such as mammalian cell toxicity effects. The drug delivery improvements from polymeric and lipid-based nanocarriers do not overcome their inability to recognize biofilm environments, which results in uncontrolled and non-

targeted drug release patterns. Several issues affect the reliable response of stimuli-responsive systems, such as pH or enzyme-activated nanocarriers, when these systems activate in heterogeneous biofilm environments. The current biofilm treatment strategies prove ineffective because they do not simultaneously address the requirements for deep biofilm penetration and extended antimicrobial action until recurrent infections emerge [20].

1.4 Research Gaps and Objectives

A wide range of nanoparticles (NPs) are currently used for treating bacterial biofilms, including nano-formulations with antimicrobial surface functionality, surface-adaptive and enzyme-responsive, stimuli-responsive NPs targeting biofilms, as well as metal and metal oxide NP formulations. These NPs mechanisms of action vary depending on the target biofilm, antibiotic type, and application method. For example, stimuli-responsive NPs are activated only under specific stimuli, such as ultrasound. However, the proposed NPs do not require external stimuli for activation. Instead, their mechanism is linked to the biofilm's natural defenses against its external environment.

To create these biologically triggerable NPs, several steps are involved. First, Carbopol's swelling ability at high pH is used to trap the antibiotic within the Carbopol polymer. Mixing the components at a pH around 8 facilitates efficient electrostatic attraction between the negatively charged dissociated carboxylic groups within the swollen Carbopol and tetracycline hydrochloride cations [3]. After encapsulation and drop of the pH to 3.33 to collapse the Carbopol nanogel, a coating with BSA is applied at low pH. BSA acts as a target for the proteases produced by the bacterial biofilm. To ensure controlled antibiotic release, the BSA is partially coated with shellac in a subsequent step. This coating helps to sustain the release of the drug within the biofilm before

the biological trigger. Shellac (ammonium salt) is dissolved at a pH of around 8 and the solution added drop-wise to the drug-loaded BSA-coated Carbopol nanoparticles. It is crucial not to overcoat the formulation with shellac, as excessive coating would prevent the bacterial proteases from reaching the BSA, thereby blocking the release of the drug. It is crucial not to overcoat the formulation with shellac, as excessive coating would prevent the bacterial proteases from reaching the BSA, thereby blocking the release of the drug. It is crucial not to overcoat the formulation with shellac, as excessive coating would prevent the bacterial proteases from reaching the BSA, thereby blocking the release of the drug. This controlled release of the antibiotic would inhibit biofilm formation by killing the bacteria and preventing the biofilm from spreading to new areas.

This novel nano-formulation not only simplifies the fabrication process but also offers significant advantages, including overcoming the antibiotic resistance of bacterial biofilms. The use of this advanced method holds great potential for effectively preventing biofilm formation and significantly reducing the existing biofilm mass by leveraging natural biofilm defenses to trigger its action. The incorporation of stimuli-responsive and enzyme-targeted functionalities, combined with controlled drug release, will enhance the efficacy of tetracycline hydrochloride in overcoming bacterial biofilm resistance.

Chapter 2

Materials and methods

2.1 Materials and Methods

Carbopol Aqua SF1 polymer (30 wt% aqueous suspension) was provided by Surfachem Group Ltd. Bovine serum albumin (BSA) standard grade with lot number CP24-7044 was provided by Capricorn Scientific. Shellac Ammonium Salt (25 wt% aqueous suspension) was kindly supplied as a gift by Stroever GmbH & Co. KG, Germany. Trypsin powder was provided by Carolina Inc. (USA). It facilitates the stereo-selective hydrolysis of amino esters and various selective esters, including heterocyclic amino esters. It was used to trigger release by digesting the BSA coating. All pH adjustments were completed using 0.25M NaOH and HCl, which were prepared in 15 mL of deionized water. HaCaT keratinocytes were obtained from ATCC (USA). Capricorn Scientific kindly provided Dulbecco's Modified Eagle Medium (DMEM) High Glucose (4.5 g/L with L-glutamine), fetal bovine serum (FBS) sterile-filtered, penicillin/streptomycin solution (100x) sterile-filtered, and trypsin-EDTA (0.05%) in HBSS (1x) with phenol red sterile-filtered, which was used to trypsinize the HaCaT cells. DMEM was made complete by mixing 500 mL DMEM, 5% FBS, and 1% penicillin-streptomycin. For the test on biofilms, a bacterial suspension of S. epidermidis was used. The nutrient broth was supplied by Carolina, while nutrient agar ISO was obtained from Condalab. Crystal Violet dye was purchased by Carolina Inc. (USA).

To obtain deionized water for this study, a water purification system Smart2Pure water purification system by Thermo Fisher Scientific was used. It applies distillation, ultra-filtration, reverse osmosis, and deionization to achieve the purity of water. To measure tetracycline hydrochloride concentration, a UV-Vis Spectrophotometer FLUOstar Omega by BMG Labtech, Ltd. (UK) was used.

The absorbance peak for this antibiotic appears at 356 nm wavelength. All experiments on the UV-Vis Spectrophotometer were conducted using a COSTAR 96- well plate from Corning. For dynamic light scattering (DLS) and electrophoretic light scattering (ELS) measurements, the Litesizer 500 from Anton Paar was used. All of the pH measurements were done using a pH meter provided by Mettler Toledo. All centrifugation was completed using a MiniSpin Plus centrifuge, which has a maximum of 14,500 rpm. This centrifuge was kindly provided by Eppendorf. All transmission electron microscopy pictures were taken using a JEOL JEM - 1400 Plus, and scanning electron microscopy pictures were taken using a ZEISS Crossbeam 540. To clean the surface of the Petri dishes, an Oxygen Plasma Cleaner from Harrick Plasma was used for 10 minutes.

2.2 Preparation of Nanoformulations loaded with Tetracycline Hydrochloride

A 0.4 wt% Carbopol stock solution was prepared by diluting 667 μL of the supplied 30 wt% Carbopol suspension to a final volume of 50 mL of deionized water. A 0.4 wt% tetracycline hydrochloride solution was prepared by dissolving 200 mg of tetracycline hydrochloride in 50 mL of deionized water. The 50 mL of 0.4 wt% tetracycline solution was then mixed with 50 mL of 0.4 wt% Carbopol nanogel suspension at pH 5 in a 100 mL beaker. The pH of the solution was then raised by gradually adding drops of 0.25 M NaOH until the solution reached pH 8 and was left under magnetic stirring for 12 hours at 400 rpm.

A 0.4 wt% BSA solution was prepared by dissolving 240 mg of BSA powder in 60 mL of deionized water at pH 3.5 without stirring to avoid foam formation. The sample was placed in a fridge until all the powder dissolved, which took approximately 1 hour. A 0.2 μm syringe filter was then used to remove large BSA aggregates from the sample.

Sixty mL of tetracycline-loaded Carbopol nanogel suspension was then mixed with 60 mL

of BSA and adjusted to pH 3.33 by gradually adding drops of 0.25 M HCl and stirred for another 30 minutes. The suspension was then centrifuged for 30 minutes at 14,000 rpm, and the supernatant was carefully collected for encapsulation efficacy analysis. The pellet was redispersed into deionized water to a final volume of 120 mL. Afterwards, the pH was adjusted to 3.33 using 0.25 M HCl drops. Finally, 0.1 wt% shellac ammonium salt was added, 1 mL at a time. It was prepared by dissolving 200 µL of 25 wt% stock shellac ammonium salt in deionized water, which was adjusted to pH 8.5. The final volume was 50 mL. After adding 42 mL of shellac ammonium salt to the tetracycline hydrochloride-loaded BSA-coated Carbopol nanogel, the pH was adjusted to 3.33 again.

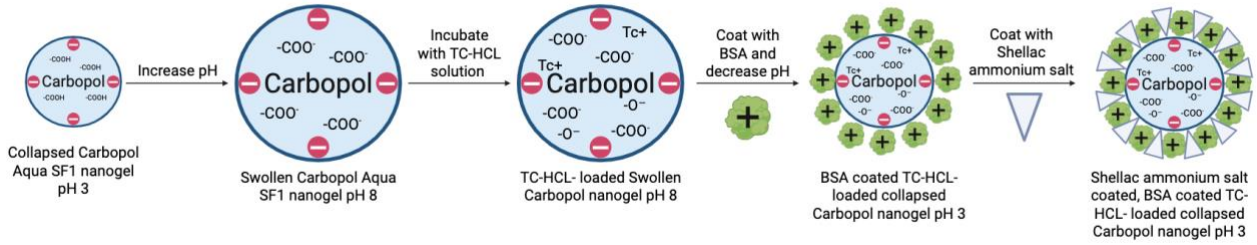

Figure 2.2. 1: Schematic representation of the loading and coating process for Carbopol Aqua SF1 nanogels with tetracycline hydrochloride (TC-HCL), BSA, and shellac ammonium salt. The process includes pH adjustments at different stages to facilitate swell

Encapsulation efficiency

To indirectly calculate the encapsulation efficiency, the absorbance of the non-encapsulated tetracycline hydrochloride was measured. This non-encapsulated drug was collected from the supernatant after the drug loading process. A calibration curve was prepared using different concentrations of tetracycline hydrochloride in range 0 μg/mL - 25 μg/mL, with all measurements taken at a wavelength of 356 nm and at pH 5.6. The encapsulation efficiency (EE) was then

calculated using the following formula:

$$\text{Encapsulation Efficiency (\%)} = \frac{[\text{Total drug} - \text{Unencapsulated drug}]}{[\text{Total drug}]} \times 100\% \qquad (2.2.1)$$

2.3 Characterization of the Nano-formulations

Particle Size and Zeta Potential Measurements

The particle size distribution, along with the zeta potential of Carbopol, BSA, shellac ammonium salt, and the complete formulation, were analyzed by dynamic light scattering (DLS) and electrophoretic light scattering (ELS) techniques using a Litesizer 500 (Anton Paar, Austria). The measurement of the average particle size and zeta potential took place at 25°C using disposable and Omega cuvettes. The refractive index and viscosity of the medium were set according to the instrument's specifications for deionized water. The refractive index of Carbopol was taken as 1.45 as for polyacrylic acid. The measurements of each sample were performed in triplicate. The instrument functioned with an equilibration period of 60 seconds, and it ran measurements for 10 seconds at a time for 30 sequential measurements.

Attenuated Total Reflectance Fourier Transform Infrared Spectroscopy (ATR-FTIR)

The chemical composition, along with the functional groups of the produced drug-loaded nanoparticles, was determined using ATR-FTIR spectroscopy. The FT-IR spectral data were recorded using a Nicolet iS10 FT-IR spectrometer combined with an attenuated total reflectance (ATR) accessory. The analysis was performed within the wavelength range from 4000 to 400 cm^{-1}. Background spectra were collected before each measurement, and all spectra were baseline-corrected and normalized using the instrument's software. The presence of characteristic absorption bands corresponding to relevant functional groups was used to confirm the drug loading and the particle coating with BSA and shellac.

Transmission Electron Microscopy (TEM)

Antibiotic-loaded coated formulations were observed for morphology, size, and structural characteristics using a Transmission Electron Microscope (TEM). The samples were prepared by diluting 100 μl of the coated formulation in 900 μl of deionized water, with the pH adjusted to 3.33. A drop of the diluted sample was placed on a copper grid coated with a carbon film, which was supplied by Agar Scientific. The TEM was performed using a JEOL JEM-1400 Plus. The microscopic analysis was performed using different levels of magnification.

Scanning Electron Microscopy (SEM)

SEM technology was used to analyze the surface and structural elements of drug-loaded Carbopol nanoparticles with BSA/shellac surface coatings. Before imaging, samples were dried onto double-sided conductive copper tape and mounted onto aluminum stubs. The Sputter-coater Q150T ES was used to enhance conductivity on the samples by applying a thin Au/Pd (60/40) layer. Analysis of samples using SEM was performed using a ZEISS Crossbeam 540. The microscope collected images at magnification levels ranging from 500x to 200,000x to assess both particle distribution and morphology, as well as the size measurement of the particles.

2.4 In Vitro Enzyme-Triggered Drug Release

Testing the enzyme-triggered release of drug-loaded nanoparticles involved using Trypsin solution. The experimental setup analyzed how Trypsin decomposes BSA while releasing the encapsulated drugs under enzymatic conditions similar to the ones in mature bacterial biofilm. A dialysis membrane containing 20 mL of drug-loaded coated nanoparticles was treated with 1% Trypsin solution while submerged in 50 mL of deionized water at a pH of 5.5–6.0. The experiments with control samples, without enzyme and uncoated drug-loaded Carbopol, were

conducted using the same stock to determine possible non-enzyme-induced drug release and the effect of coating on drug release. The samples were incubated with 100 rpm magnetic stirring at room temperature for 41 hours. During the incubation, 1 mL of solution was collected at specific time points, including 5, 15, and 30 minutes, 1, 2, 3, 6, 12–14, 23, and 24 hours. After each collection, 1 mL of deionized water was immediately added to the surrounding water. The drug concentration was measured by UV-Vis spectrophotometry. The cumulative release profile was obtained by plotting the amount of released tetracycline hydrochloride as a function of time.

2.5 In Vivo Bacteria Triggered Drug Release

Preparation of Petri dishes with particles

Sixty mm non-treated Petri dishes were plasma cleaned in an oxygen plasma cleaner for 15 minutes on a medium power setting. Aliquots of 0.1, 0.2, 0.3, 0.5 mL of coated unloaded NPs (0.0741 wt% Carbopol + 0.1481 wt% BSA + 0.0259 wt% Shellac), uncoated tetracycline-loaded NPs (0.0741 wt% Carbopol + 0.0741 wt% tetracycline hydrochloride), and coated tetracycline-loaded BSA nanoparticles (0.0741 wt% Carbopol + 0.1481 wt% BSA + 0.0259 wt% shellac + 0.0741 wt% tetracycline hydrochloride) were poured into Petri dishes. The plates were dried in an UNITEMP Drying Cabinet on mode 3. Then the same aliquots of these particles were poured into other oxidized Petri dishes, which were not air-dried. DI water was added to these plates to top up the volume of each particle solution to 1.5 mL.

Preparation of S.epidermidis biofilm

A single colony of *S. epidermidis* from the stock was inoculated in 20 mL of nutrient broth in a sterile 50 mL Falcon tube one day prior to culturing bacteria with nanoparticles. The tube was incubated overnight (O/N) in the shaking incubator at 37°C. The next day, the concentration of the

bacterial suspension was measured using a FLUOstar Omega at 600 nm wavelength and adjusted to OD600 = 0.1. Then, 3 mL of the bacterial suspension was poured into control Petri dishes (without nanoparticles) and Petri dishes with nanoparticles. The dishes were incubated for 24 hours at 37°C. After incubation, the bacterial suspension was removed from all plates. The Petri dishes were washed with deionized water twice. Half of the plates were used for the Crystal Violet (CV) assay, while the other half were used for CFU counting.

CV assay

3 mL of CV solution was added to the washed Petri dishes. After 40 minutes, the CV solution was discarded into a waste beaker with bleach, and the plates were washed with deionized water twice. After drying, 3 mL of 30% acetic acid was poured into the Petri dishes, mixed, and left for 10 minutes. Then, 200 µL of controls and all samples were transferred to a COSTAR 96-well plate in triplicates, and optical density was measured using UV-Vis spectrophotometry. Finally, the residual biomass was calculated using the obtained values.

CFU count

PBS was added to the washed Petri dishes. 2 mL of diluted ultrasonic gel was poured into zip packages. The plates were placed into these packages, and the gel was spread over the bottom surface of the Petri dishes. The same amount of gel was applied to the 1 MHz ultrasonic head. The cavitation effect instrument was set to partial power, and the Petri dishes were sonicated for 5 minutes with the 1 MHz ultrasonic head. After sonication, PBS from all Petri dishes was transferred into sterile 5 mL Eppendorf tubes. Then, 4 sterile Eppendorf tubes were labeled with dilution factors 10^1, 10^2, 10^3, and 10^4 for all samples, and 900 µL of sterile PBS was pipetted into all four Eppendorf tubes. The original solutions of each sample and control in 5 mL Eppendorf

tubes were vortexed and then serially diluted from 10^1 to 10^4 using 100 µL aliquots, with vortexing after each dilution. After this, NA plates were divided into 4 sectors and labeled from 10^1 to 10^4. 10 µL from each dilution was plated on NA in the respective sectors for all samples. The plates were incubated overnight at 37°C. The next day, colonies in each sector were counted for all samples, and CFU/mL was determined.

2.6 Cytotoxicity on Human Keratinocytes

Cell harvesting is performed first to separate HaCaT cells from their culture surface using trypsin treatment. A fixed number of cells is distributed between two separate 96-well TC- treated plates for MTS cell proliferation assessment and Hoechst/PI cell viability testing. Each well received complete DMEM solution containing no Phenol Red to prevent absorbance measurement interference later. The culture incubation under temperature conditions of 37°C with 5% CO_2 leads to well surface attachment of cells to the wells bottom for 24 hours.

MTS proliferation Assay

After the completion of the cell attachment phase, the next step is to treat the cells with drug-loaded nanoparticle solutions. The total volume for each well reaches 100 μL after adding the solution. The test wells receive medium alone, while the experimental wells receive nanoparticle suspensions in increasing concentrations of 10 μL, 20 μL, and 30 μL. The preparation process starts with the dilution of the nanoparticle suspension in the medium until the total volume in each well reaches 100 μL. The experiment includes triplicates for each treatment condition to achieve reliable statistical results. Cells in the plates experience nanoparticle interaction during a second 37°C incubation period that lasts 24 hours. The next step is to carefully aspirate the medium from all wells, followed by the distribution of fresh phenol red-free DMEM to all wells.

The analysis for MTS proliferation tests requires the direct application of MTS reagents into individual wells. Absorbance was measured at Time 0 before the plate continues incubating for one more hour. The examination of cell metabolic activity as an indicator of cell proliferation occurred through another absorbance measurement after 1 hour of incubation. The extension of the incubation time up to two hours was performed to enhance data reliability, and blank wells will be used to account for background absorbance levels.

The Hoechst/PI cell viability assay

The Hoechst/PI viability assay requires preparing PBS solutions of staining reagents, which are added as 10 μL Hoechst and 13 μL PI to the wells. The cells require a 30-minute incubation under room temperature conditions with light protection before they are examined with a fluorescence microscope. The Hoechst staining solution shows blue fluorescence when it binds to the DNA in all cell nuclei, while the PI staining solution shows red fluorescence when it attaches to the DNA in dead cell nuclei as it can penetrate only cells with compromised membranes. The technique provides live cell identification, along with the detection of percentage of dead cells in each well. To calculate Hoechst/PI assay viability results, the following method should be used:

$$Viability\ (\%) = \left(\frac{Hoechst^{+}PI^{-}\ cells}{Total\ Hoechst^{+}\ cells}\right) \times 100\% \qquad (2.6.1)$$

2.7 Statistical Analysis

All data were expressed as the mean ± standard deviation (SD). Statistical analysis was performed using Microsoft Excel. All experiments were conducted in duplicate or more.

Chapter 3

Results and Discussion

The experimental analysis of the developed nano-formulation presents results that focus on its characterization, release mechanism, and effect on the bacterial biofilm. The nano-formulation comprises tetracycline hydrochloride-loaded in Carbopol nanogel, followed by a BSA and shellac coating. The multiple layers within this design serve as an essential element of the controlled drug release system.

In the first part, the characterization of the individual components as well as the final loaded and coated nano-formulation is described. Particle size measurement, zeta potential determination, and surface morphology evaluation of the nano-formulation are conducted. The stability and integrity of the nano-formulation can be inferred from these characteristics, ensuring the components remain in a well-organized and effective state.

In the second section, the focus shifts to the release profile of the nano-formulation. When the bacterial proteases, generated within the EPS, digest the BSA component of coating, the encapsulated antibiotic release mechanism is triggered as the shell turns leaky. As a result of this mechanism, tetracycline hydrochloride is released from the formulation in the presence of proteases in the environment. If the protease is not active, small amounts of the antibiotic are still released but at a much lower rate. However, in the presence of Trypsin, an increased dose of tetracycline is released. This mechanism results in the formulation having a better therapeutic effect under the specific conditions where bacterial biofilm formation and protease production are present. The antibiotic release profile of the biologically triggered nano-formulation is compared with an uncoated drug-loaded Carbopol and the coated drug-loaded complete formulation, showing it to be more controllable

and responsive.

The third section evaluates the in vivo efficacy of the nano-formulation in treating biofilm-related infections using *S. epidermidis* as the model pathogen. Petri dishes containing biofilms were incubated with bacterial suspensions containing drug-loaded and unloaded nanoparticles. The crystal violet (CV) assay was used to test the effectiveness of this formulation for measuring the residual biofilm biomass, and colony-forming unit (CFU) counts were done to quantify bacterial growth.

The final section presents the results of the cytotoxicity assessment of the nano-formulation on HaCaT cells. The purpose of this evaluation was to determine the safety of the nano-formulation for potential clinical applications. HaCaT cells were exposed to varying concentrations of drug-loaded and unloaded nanoparticles.

All the presented results highlight the potential of the multi-layered nano-formulation to provide targeted, controlled antibiotic release in response to bacterial activity, demonstrating its effectiveness in both in-vitro and in-vivo environment. The formulation offers a promising approach for treating biofilm-related infections, with enhanced therapeutic efficacy and a favorable safety profile for clinical applications.

3.1 Characterization of Nano-formulations

Particle Size and Zeta Potential Measurements

Figure 3.1.1 presents the hydrodynamic size and zeta potential of Carbopol at different pH levels (ranging from pH 3 to pH 9). The samples were prepared by dissolving Carbopol in deionized water at a concentration of 0.1 wt% and adjusting the pH using NaOH and HCl. Hydrodynamic size and zeta potential were determined using a Litesizer 500 by Anton Paar, with each measurement taken three times for accuracy.

The data in Figure 3.1.1 reveal distinct trends for both hydrodynamic size and zeta

potential across the different pH levels. The hydrodynamic size of Carbopol was 100 ± 7.64 nm at pH 3, and no distinct changes were observed at other low pH points. However, as the pH increased to pH 6 and above, the hydrodynamic size increase was significant, reaching around 294 ± 4.84 nm at pH 7. The hydrodynamic size reached 378 ± 15.69 nm, significantly increasing at pH 9. Therefore, the pH effect on the particle size of Carbopol indicates that the particle size increases with increasing pH, which is due to the swelling of the polymer at higher pH.

Carbopol polymer show this behavior because its carboxylic acid groups become ionized at higher pH. Under acidic conditions, when carboxyl groups (-COOH) exist mainly in their protonated form, the electrostatic repulsion force between polymer chains remains low. The polymer chains stay tightly folded, which keeps the hydrodynamic size small (around 100nm). Increased pH conditions cause the carboxyl groups to lose their protons, thereby turning into negatively charged carboxylate ions ($-COO^-$). Backbone expansion, along with water absorption, occurs because electrostatic repulsions between polymer chains increase [3].

In contrast, zeta potential measurements showed an inverse trend. The surface charge on the Carbopol particles, as revealed by the zeta potential measurements, was comparatively high at pH 3 (-25 mV). An increase in pH to 4.5 resulted in a more negative zeta potential, with a value of around -35 mV. Of particular interest, the zeta potential became increasingly more negative as pH increased up to and beyond pH 6. At pH 6.5, the negative value approached -50 mV. These results suggest that Carbopol nanogel particles become more highly negatively charged at higher pH due to the dissociation of polymer carboxyl groups.

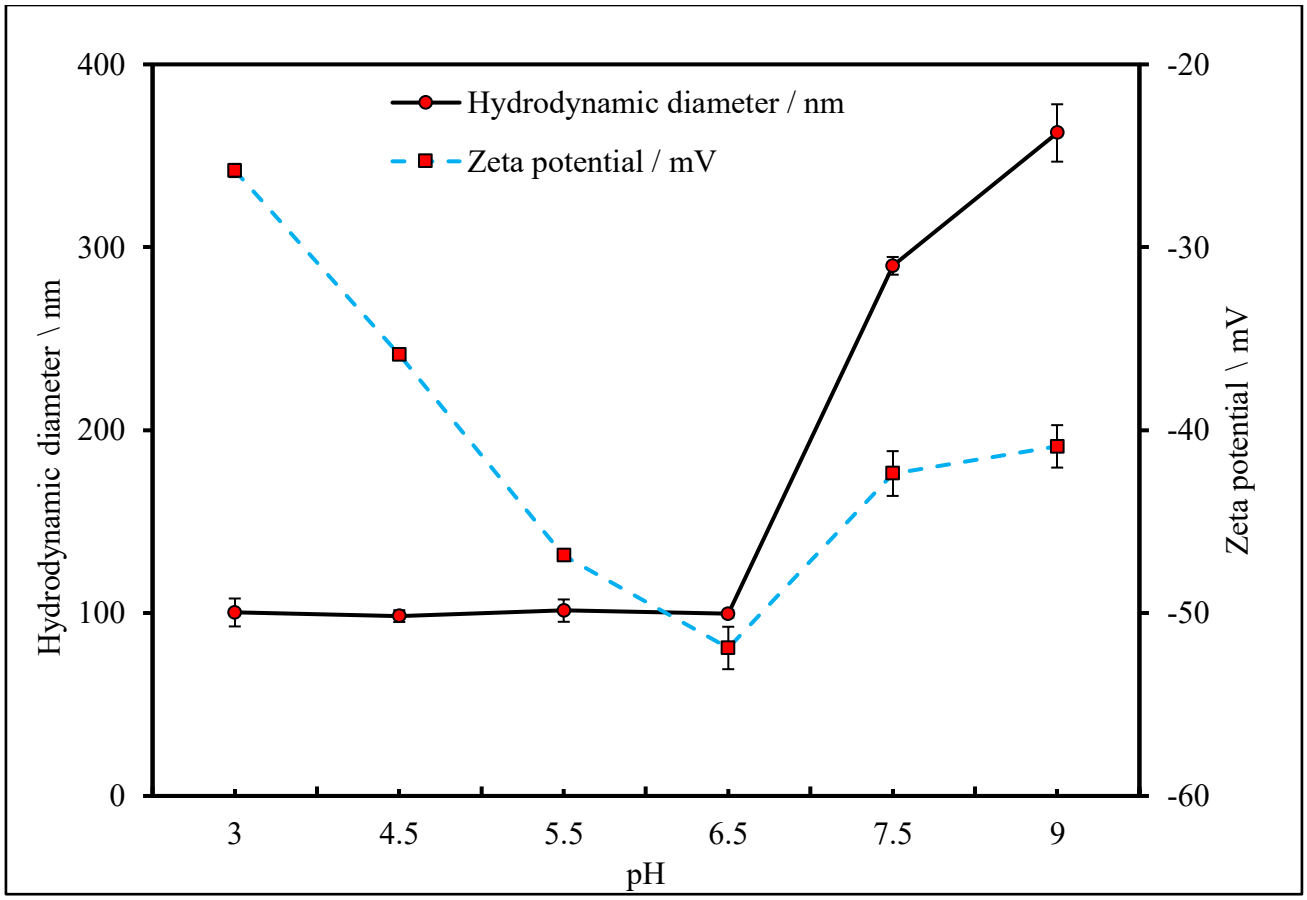

Figure 3.1. 1: Average hydrodynamic diameter and zeta potential distribution of Carbopol Aqua SF1 nanogel in different pH levels.

The hydrodynamic diameter and zeta potential of BSA were measured over a range of pH values to determine the effect of pH on BSA. As shown in Figure 3.1.2, the hydrodynamic diameter of BSA nanoparticles decreased with increasing pH, from 3 to 9. At pH 3, the hydrodynamic diameter was approximately 8.5 nm, which progressively reduced to around 2 nm at pH 9.

In contrast, the zeta potential showed an inverse trend to the hydrodynamic diameter. At pH 3, the zeta potential was highly negative. This indicates that the BSA protein molecules had a strong surface charge, which contributes to their stability. The zeta potential decreased with increasing pH and became more negative, reaching -28 mV at pH 7 and then tending to -35 mV at pH 9. It should also be noted that the isoelectric point of BSA is between pH 4.3 and 4.5.

The changes are due to the impact of pH on both amino ($-NH_2$) and carboxylic acid (-COOH) functional groups within BSA molecules. The majority of carboxylic acid groups exist in their protonated form (-COOH) at low pH, while amino groups exist as positively charged ammonia groups ($-NH^+$). As a result, a positively charged surface forms, which leads to reduced molecular repulsion, while the protein partially unfolds and increases its hydrodynamic size. However, when the pH level passes the isoelectric point, carboxylic acid groups (-COOH) lose their protons and become negatively charged carboxylate ions ($-COO^-$), while amino groups lose their positive charges. The protein surface becomes negatively charged as the pH rises above the isoelectric point, which leads to the observed negative zeta potential value. Strong electrostatic repulsions between BSA molecules occur due to the increasing negative charge, which inhibits aggregation and allows the protein to maintain a compact, stable conformation. The recorded decrease in hydrodynamic diameter occurs as a result of these changes [21].

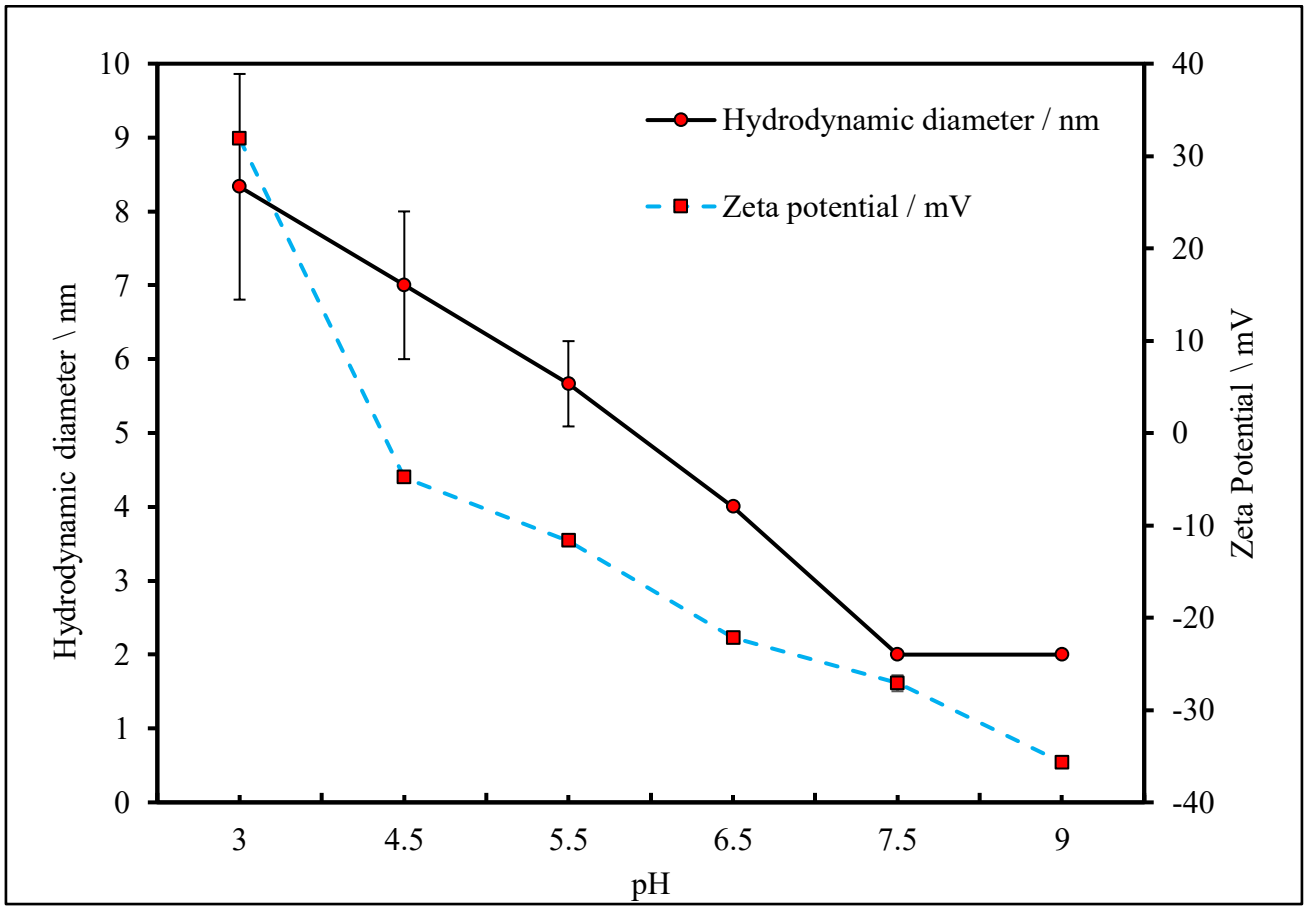

Figure 3.1. 2: Average hydrodynamic diameter and zeta potential distribution of BSA in different pH levels.

The hydrodynamic diameter and zeta potential of precipitated shellac at low pH were determined to examine the effect of pH on the zeta-potential of the shellac surface. Figure 3.1.3 shows a significant decrease in the hydrodynamic diameter of shellac particles with increasing the pH from 3 to 5. At pH 3, the hydrodynamic diameter was approximately 1,400 nm, which rapidly reduced to around 800 nm by pH 5.5. This very rapid drop suggests a significant pH-induced conformational change or aggregation behavior, where protonation and electrostatic interactions in the shellac take place. It was found that after pH 6.5, the hydrodynamic diameter remained relatively stable within the range of 100 nm to 60 nm. Regarding the zeta potential, it exhibited an inverse trend to the hydrodynamic diameter. At pH 3, the zeta potential was slightly positive, around +6 mV. From pH 3

through 5, the zeta potential became more negative and stabilized around -20 mV. Little change in zeta potential occurred at higher pH values. Overall, the results indicate clear trends of pH dependence for shellac.

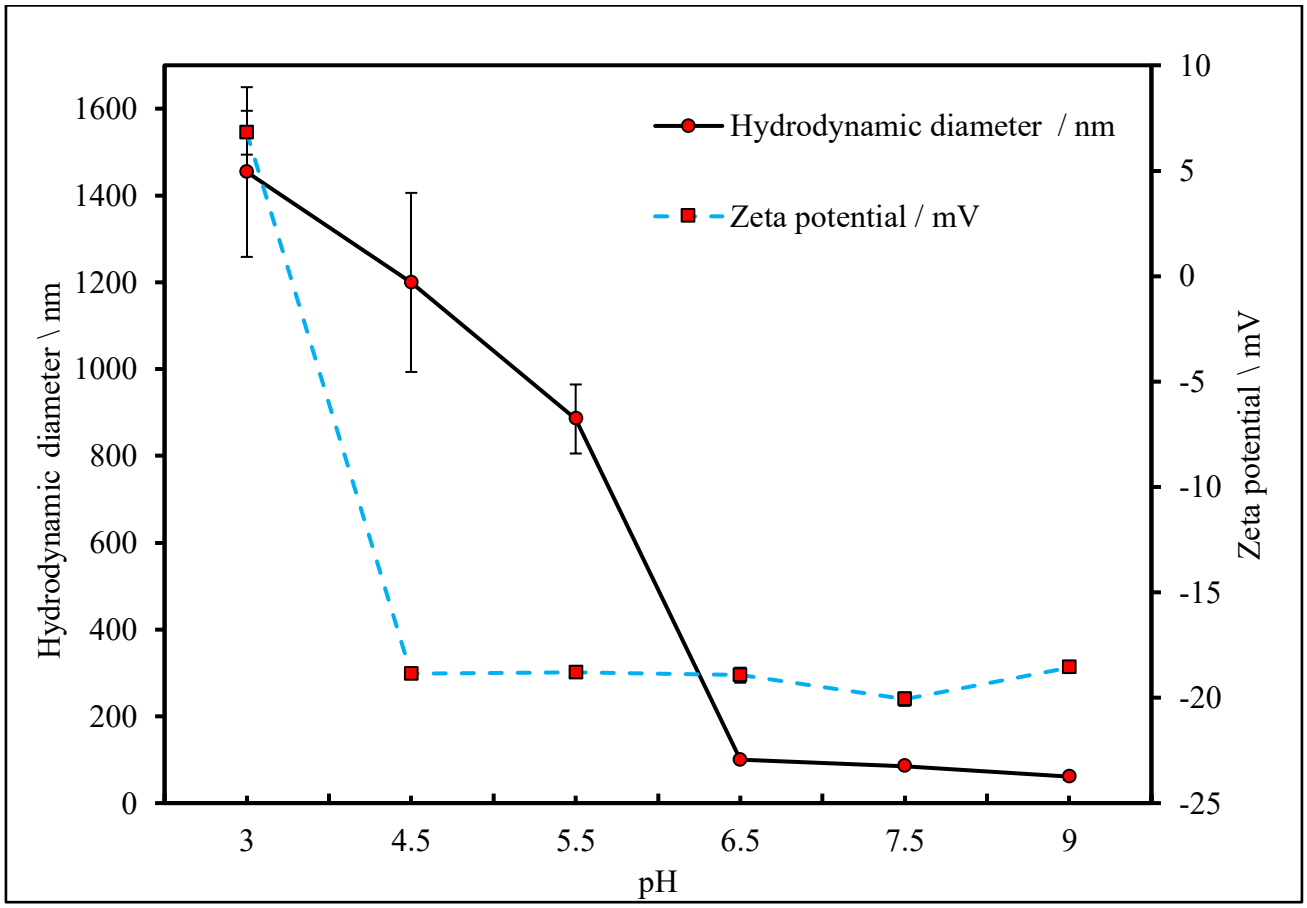

Figure 3.1. 3: Average hydrodynamic diameter and zeta potential distribution of shellac in different pH levels.

ATR-FTIR

In Figure 3.1.4, the FTIR spectra of the individual components, as well as the formulation, are shown. A number of significant features are present in the spectrum of tetracycline hydrochloride. The presence of hydroxyl groups is indicated by a broad O-H stretching vibration at 3285 cm^{-1}. Furthermore, typical aliphatic C-H stretching vibrations occur at 2959 cm^{-1}. There is a peak at

1640.41 cm^{-1} that is attributed to a carbonyl group with a significant C=O stretching vibration. In addition, the presence of methyl and ether groups is also confirmed by C-H bending at 1387 cm^{-1} and C-O bending at 1239 cm^{-1}. These FTIR results are consistent with those reported by Trivedi et al. (2015), who also identified the same key functional groups in tetracycline [22].

In agreement with the presence of hydroxyl groups in the polymer, a broad O-H stretching vibration appeared at 3288 cm^{-1} in the Carbopol spectrum. The C-H stretching vibration occurs at 2929 cm^{-1}, while the C=O stretching at 1702 cm^{-1} is characteristic of a carbonyl group in Carbopol. The C-H bending at 1446 cm^{-1} is associated with methylene and methyl groups.

Characteristic of secondary protein structure, including amide I (1640 cm^{-1}) and amide II (1550 cm^{-1}) bands, can be seen in the BSA spectrum. These come from the C=O stretch (amide I) and C-N stretch (amide II), suggesting beta sheets and alpha helices, which are common protein conformations. Functional groups that could potentially interact with the formulation components can be inferred from the peaks between 500–1500 cm^{-1}. The FTIR analysis results matched Oudemans et al.'s (2007) findings about BSA which showed Amide I, II and C–H bending bands indicating usual protein secondary structures [23].

A broad O-H stretch at 3346 cm^{-1} is present in the Shellac spectrum, which is common to hydroxyl groups. The C-H stretch at 2926 cm^{-1} is characteristic of aliphatic hydrocarbons, while the C=O stretching at 1703 cm^{-1} corresponds to ester groups, which is a defining feature of Shellac. C-H bending at 1458 cm^{-1} and C-O-C bending at 1250 cm^{-1} are typical of ether groups. These spectral features are consistent with the findings reported by Chen et al. (2024), who similarly identified hydroxyl, ester, and ether groups in Shellac using FTIR analysis [24].

The formulation spectrum exhibits overlapping features of all components, confirming the

presence of Carbopol, BSA, tetracycline hydrochloride, and Shellac. Strong C=O stretching at 1710 cm^{-1} can be seen due to contributions from BSA (amide I), Carbopol (carboxyl groups), Shellac (ester groups), and tetracycline (carbonyl groups). The peaks occurring at 1504–1448 cm^{-1} support the contribution of BSA and Shellac based on C-H bending and amide II bands. From the broad O-H/C-H stretch at 2922 cm^{-1} and the C-O stretching bands at 1250–1017 cm^{-1}, Carbopol, Shellac, and tetracycline were validated. Moreover, small shifts in peak positions imply that there are hydrogen bonding and electrostatic interactions between these components in the formulation.

The FTIR analysis also reveals several interactions in the formulation. The O-H stretch at around 3280 cm^{-1} and the C=O stretch at 1700 cm^{-1} are suggestive of hydrogen bonding between the hydroxyl groups of tetracycline and Carbopol, as well as the ester groups of Shellac. In separate form, BSA exhibits the amide I band around 1650 cm^{-1} and the amide II band around 1540–1550 cm^{-1}. These amide I and amide II bands shift to 1710 cm^{-1} and around 1504 cm^{-1}, respectively, in the formulation spectrum. This shift occurs because the electron environment surrounding the peptide bonds is altered due to the electrostatic interaction of the negatively charged carboxylate groups of Carbopol and the positively charged amino groups of BSA. Moreover, the peaks in the 1700–1500 cm^{-1} region also broadened, further supporting the complex formation of Carbopol and BSA. Overall, the FTIR analysis confirms that BSA, Carbopol, Shellac, and tetracycline hydrochloride are present in the formulation.

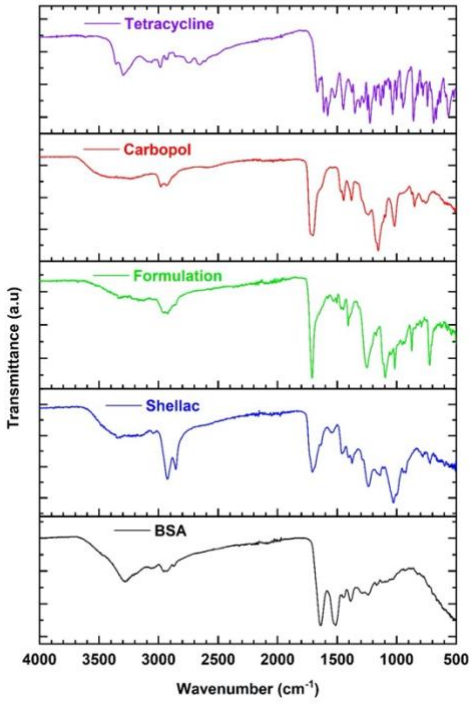

Figure 3.1. 4: ATR-FTIR Spectroscopy of Individual Components and Formulation

TEM Imaging

TEM imaging was performed to observe the morphology of Carbopol particles and the effects of coating with BSA and Shellac. The images presented in Figure 3.1.5 provide insight into the structural characteristics of the particles. In Panel A, the TEM image of Carbopol particles shows a relatively uniform, spherical morphology with particle sizes of 136 nanometers. These particles appear smooth and rarely aggregated, indicating the characteristic form of Carbopol without any surface modifications. Panel B presents the TEM image of BSA, revealing smaller, discrete particles compared to Carbopol. The BSA particles are clearly defined, with a size range of approximately 6–7 nm. In Panel C, the BSA-coated Carbopol particles are shown. The image demonstrates a well-defined spherical particle structure with a visible coating layer, suggesting the successful coating of BSA around the Carbopol core. Panels D and E show TEM images of Shellac and BSA-coated Carbopol particles. The particles show a uniform spherical shape with a thicker coating compared to

the BSA-only formulation. These images suggest that Shellac may form a more rigid and stable outer layer around the Carbopol core, possibly enhancing the structural integrity and controlled release properties of the particles. The particle size is again slightly larger compared to the BSA-coated Carbopol, indicating the additional coating layer of Shellac.

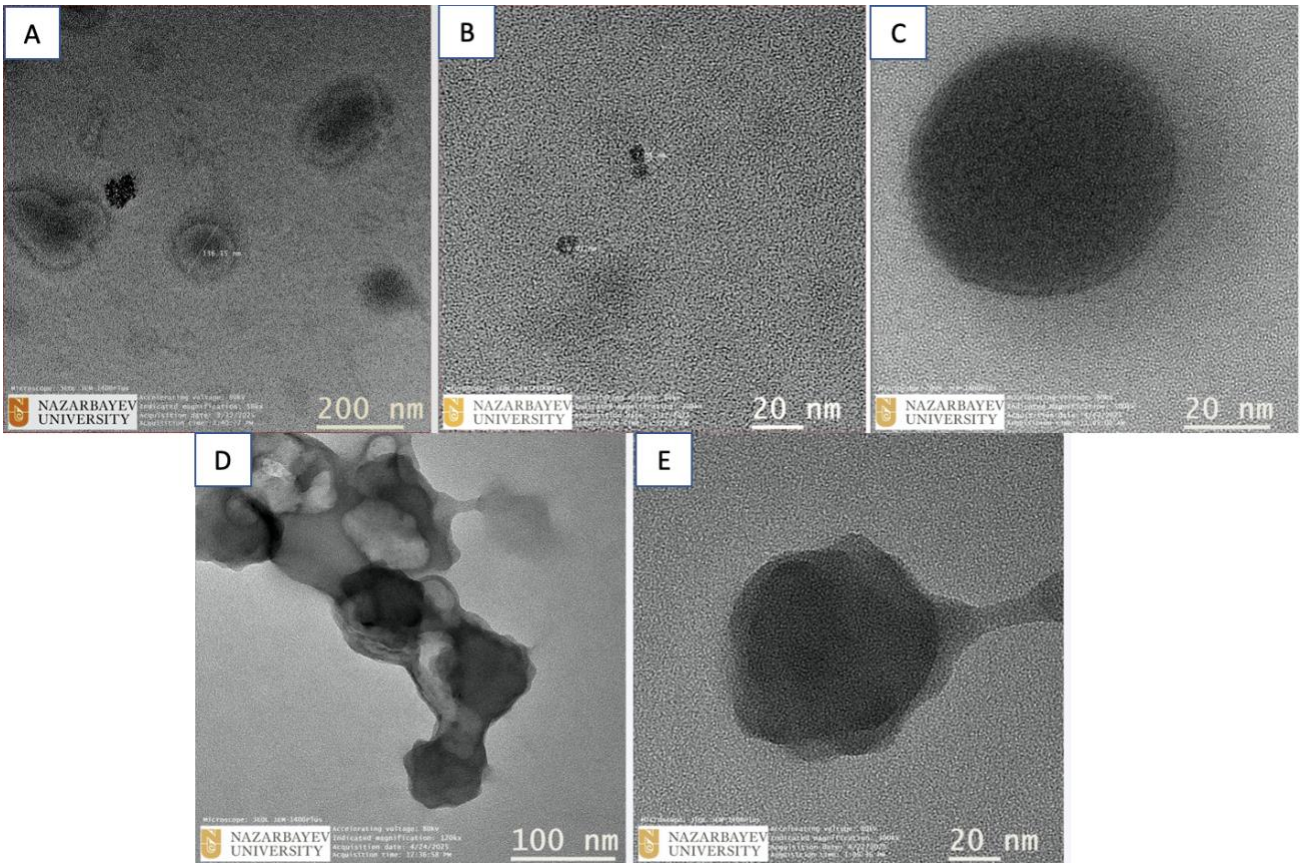

Figure 3.1. 5: Morphological imaging of BSA and shellac coated Carbopol particles. Representative TEM image of a sample of (A) Carbopol only, (B) BSA only, (C) BSA coated Carbopol, and (D,E) shellac/BSA coated Carbopol.

SEM Imaging

The surface characteristics of Carbopol and BSA-Shellac-coated Carbopol particles were examined using SEM, as shown in Figure 3.1.6. Panel A presents the SEM image of Carbopol particles, which display a spherical morphology with an average particle size ranging from approximately 80 to 100 nm. The particles appear smooth and uniform, indicating the characteristic structure of pure Carbopol without any surface modifications.

In Panel B, the SEM image of BSA and Shellac-coated Carbopol particles is shown. These particles exhibit a similar spherical shape but with a slightly larger particle size compared to the Carbopol-only particles. Additionally, the particles appear rough and highly interconnected, indicating that the surface coating of BSA and Shellac successfully modified the surface of the Carbopol particles.

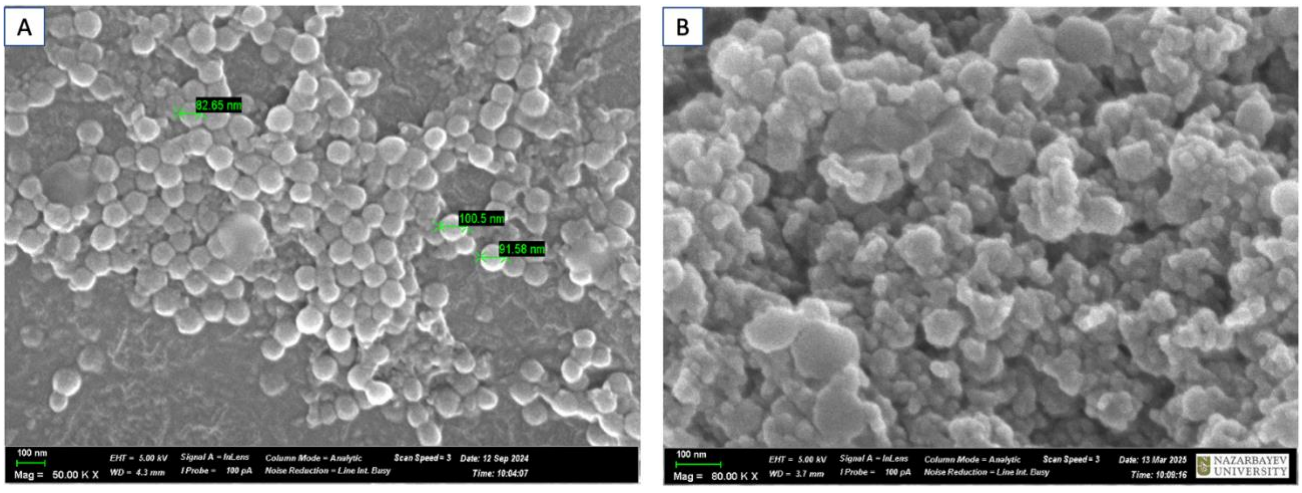

Figure 3.1. 6: SEM Imaging of (A) Carbopol and (B) BSA-Shellac-Coated Carbopol Particles.

3.2 Preparation of Tetracycline Hydrochloride loaded Nano-formulations

The hydrodynamic diameters of the various drug-loaded nano-formulations were measured and are presented in Figure 3.2.1. The results indicate that the size of the nanoparticles varies depending on the coating. The tetracycline hydrochloride-loaded Carbopol particles had an average hydrodynamic diameter of approximately 126 ± 3.1 nm. When the formulation was coated with BSA, the particle size slightly increased to around 134 ± 5.0 nm. This increase in size suggests that the BSA coating contributes to the overall particle size by forming a layer around the Carbopol nanoparticles. Furthermore, the incorporation of Shellac coatings resulted in a further increase in particle size, with the hydrodynamic diameter reaching approximately 153 ± 6.7 nm. This suggests that the Shellac coating, in combination with BSA, contributes to a larger particle size compared to the BSA-only coating, likely due to the additional layer and possible changes in the polymer matrix. Overall, the data from Figure 3.2.1 demonstrate that the size of the drug-loaded nanoparticles increases with the addition of BSA and Shellac coatings, indicating successful surface modifications and the potential for controlled drug release.

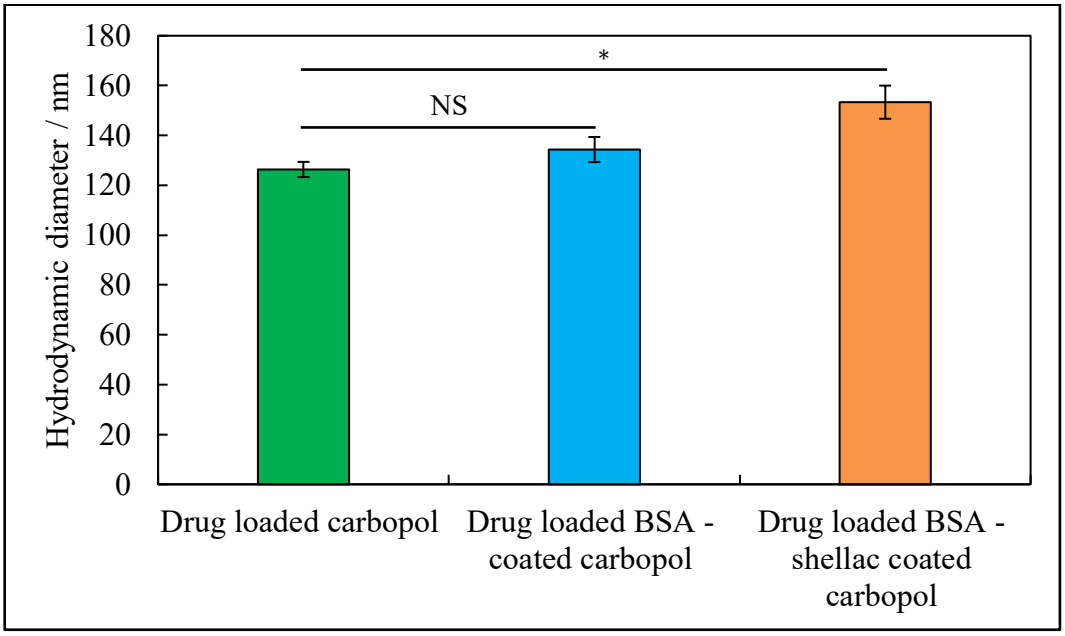

Figure 3.2. 1: Hydrodynamic Diameter of Drug-Loaded Carbopol, BSA-Coated Carbopol, and BSA-Shellac Coated Carbopol Nanoparticles at pH 3.33.

The zeta potential of the drug-loaded nano-formulations was evaluated and is presented in Figure 3.2.2. The data indicates significant differences in the surface charge of the formulations based on the presence of surface coatings. The zeta potential measurement of drug-loaded Carbopol nanoparticles showed a highly negative charge at -30 ± 0.5 mV because Carbopol nanoparticles naturally carry a negative zeta potential due to their carboxyl groups. BSA coating of Carbopol nanoparticles led to a transformation in zeta potential from negative values to +31 ± 0.8 mV. The system showed a minimal reduction in surface charge after the addition of Shellac coating. The zeta potential measurement of the final formulation showed +26 ± 1.4 mV. Measurements of the zeta potential confirm that both BSA and Shellac surface coatings modify drug-loaded Carbopol nanoparticles.

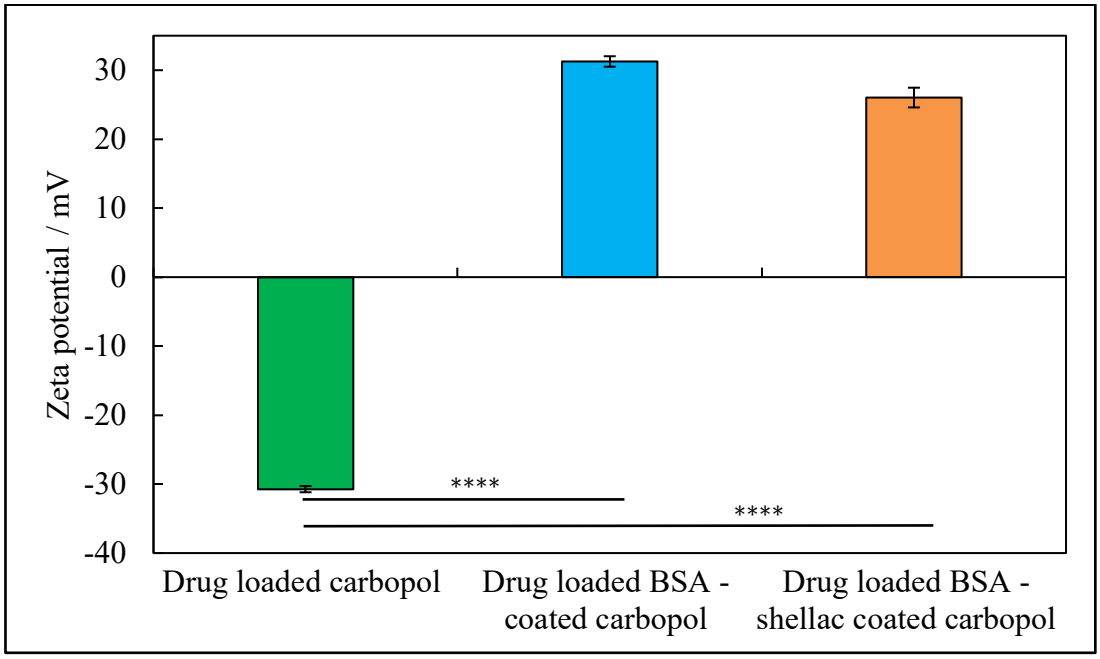

Figure 3.2. 2: Zeta potential of Drug-Loaded Carbopol, BSA-Coated Carbopol, and BSA-Shellac Coated Carbopol Nanoparticles at pH 3.33.

Encapsulation efficiency

The encapsulation efficiency measurements for tetracycline in nanoparticles were performed after an overnight drug loading process, followed by BSA addition and subsequent centrifugation. Tetracycline had an initial concentration of 4000 μg/mL before encapsulation, while 659 μg/mL of the drug remained in free form after processing. The two experimental trials achieved an encapsulation efficiency rate of 83.08% ± 0.64%, reflecting substantial tetracycline uptake by the nanoparticles.

3.3 In Vitro Enzyme-Triggered Drug Release

Tetracycline-loaded BSA/Shellac-coated Carbopol released the drug at a slow rate with minimal total drug output. The formulation achieved its greatest drug level of 6 μg/mL after 41 hours. The tetracycline hydrochloride-loaded Carbopol formulation released the drug at a significantly faster rate compared to the tetracycline hydrochloride-loaded BSA and Shellac-coated Carbopol

formulation. The incorporation of BSA and Shellac into the formulation affected its structural organization, reducing the dispersal of drug compounds until the tetracycline-loaded Carbopol formulation released 10.5 μg/mL of drug material after 41 hours. When 1% trypsin was added to the tetracycline hydrochloride-loaded BSA/Shellac-coated Carbopol system, it resulted in a release profile initially similar to the coated nano-formulation but later converged drug-loaded non-coated Carbopol system. The drugs in the formulation experienced accelerated release because trypsin caused BSA degradation through proteolytic activity, which increased the BSA/shellac shell porousness. When trypsin was present, it caused a rapid increase in drug concentration, producing drug release at a slightly better level than the non-enzymatic system, reaching 10.2 μg/mL of tetracycline hydrochloride after 41 hours. Tsigara et al. (2023) reported that tetracycline has a minimum inhibitory concentration (MIC) of 1.32 µM for *S. epidermidis*, while the minimum bactericidal concentration (MBC) is 171.4 µM [25]. Comparing the experimental results with the presented data, the tetracycline-loaded BSA/shellac-coated Carbopol system releases enough antibiotic to inhibit bacterial growth, while it is insufficient to achieve full bactericidal action.

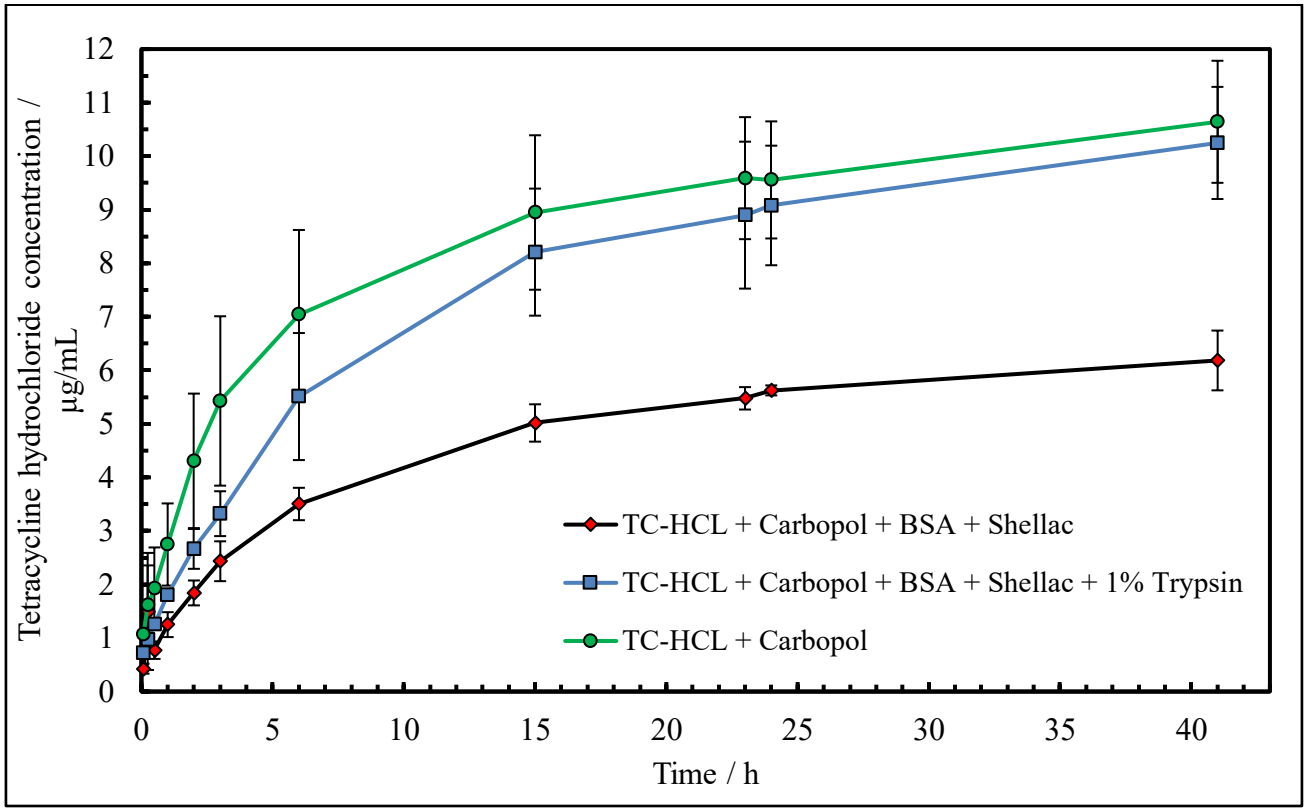

Figure 3.3. 1: Tetracycline release kinetic curve of the (i) non coated loaded Carbopol, (ii) BSA/shellac coated TC loaded Carbopol and (iii) the BSA/shellac coated TC loaded Carbopol in the presence of 1 wt% trypsin over the course of 41 hours.

3.4 In Vivo Bacteria Triggered Drug Release

The drug release profiles were evaluated using the CV assay, where residual biomass was measured after exposing various formulations dried on Petri dish to bacterial biofilm. The formulations tested included both drug-loaded and unloaded coated formulations, as well as drug-loaded Carbopol formulations. The control group, which did not undergo treatment, exhibited the highest residual biomass (100%) and served as a baseline for comparison. For the drug-unloaded formulations, a gradual decrease in residual biomass was observed as the volume of the formulation increased. Specifically, the formulation with 1.5 mL showed the most significant reduction in biomass. In contrast, the drug-loaded Carbopol formulations demonstrated a more significant decrease in

biomass compared to the unloaded formulations. The greatest reduction in residual biomass was observed in the 1.5 mL formulation, which exhibited approximately 15% residual biomass. This result highlights the effectiveness of the antibiotic in bacterial biofilm treatment. Similarly, the drug-loaded coated formulations showed a more pronounced reduction in residual biomass compared to both the unloaded coated formulations and the drug-loaded Carbopol formulations. The drug-loaded coated formulations, particularly at 1.0 mL and 1.5 mL volumes, demonstrated the most effective release, with the highest drug release observed in the 1.5 mL formulation. The increase in residual biomass reduction with larger volumes can be attributed to the formation of a more porous EPS, likely due to enzyme-induced degradation of BSA, which allowed for accelerated antibiotic release.

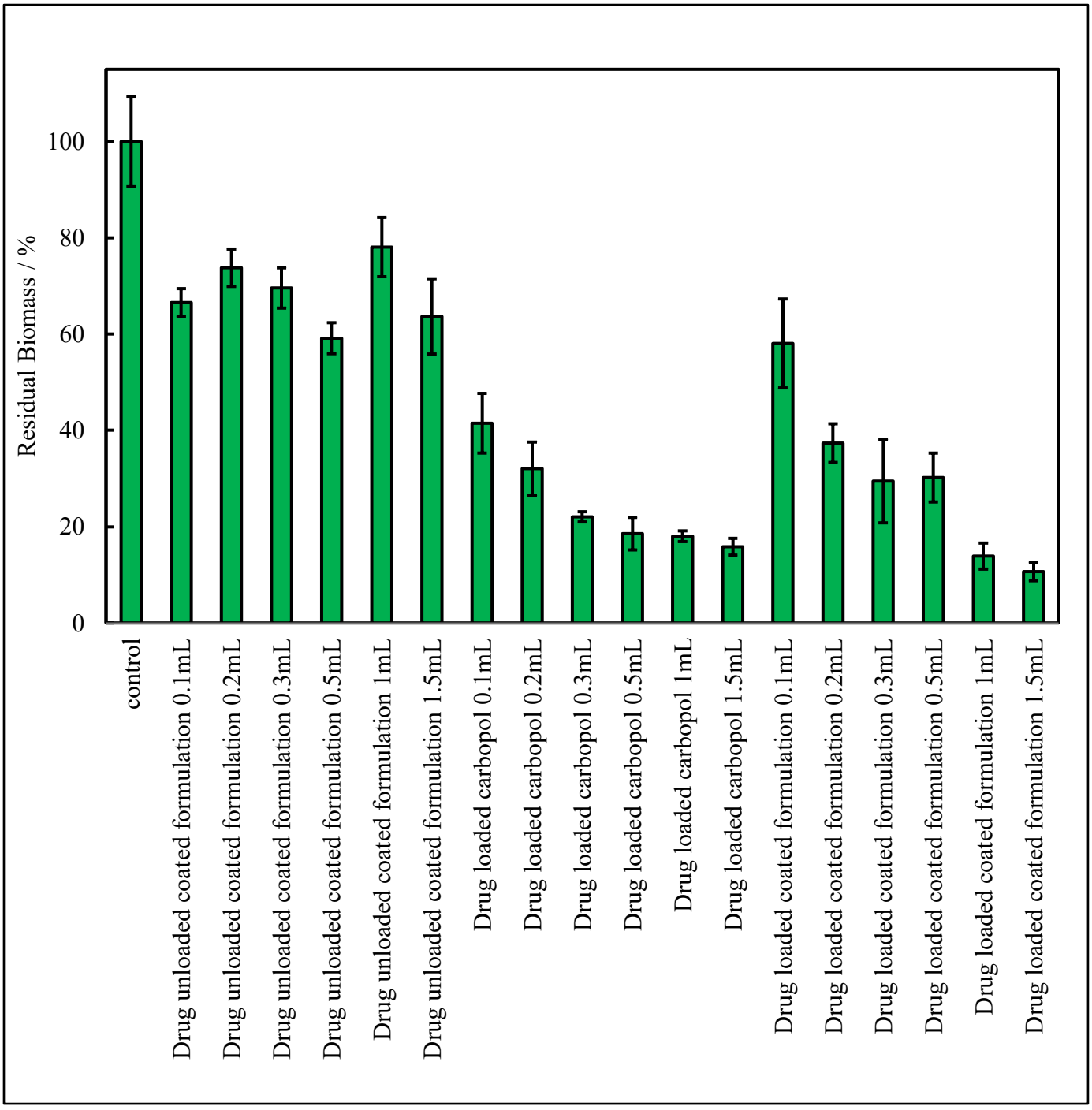

Figure 3.4. 1: Percentage of residual bacterial biofilm from S. epidermidis following 24h of growth under a variety of treatments with different air-dried aliquots of air dried non-loaded coated Carbopol, loaded non-coated Carbopol and loaded coated with BSA/shellac.

The effectiveness of drug-loaded and unloaded formulations was assessed through a CFU count test, as shown in Figure 3.4.2. The control group, which did not receive any treatment, showed the maximum CFU count per mL, indicating active bacterial growth. Drug-loaded Carbopol formulations and drug-loaded BSA-Shellac-coated particles achieved superior bacterial growth reduction compared to the control group. This was observed using high concentration doses (0.5–1.5 mL). The drug-loaded Carbopol formulations displayed the most significant CFU count reduction, with aliquots of 0.5 to 1.5 mL per 3 mL bacterial broth in the Petri dish showing the minimal bacterial growth. This suggests that the drug-loaded Carbopol formulation effectively inhibited bacterial growth at higher concentrations. The drug-loaded coated formulations also demonstrated reduced bacterial growth. An increase in the concentration level from 0.5 to 1.5 mL resulted in a decrease in the CFU count and led to lower values compared to the control and unloaded formulations. In comparison, drug-unloaded coated formulations exhibited a minimal reduction in bacterial growth, similar to the control group, indicating that the coatings alone did not significantly affect bacterial viability. Overall, the data suggest that drug-loaded formulations, particularly those with higher aliquots, exhibited the most effective antimicrobial activity.

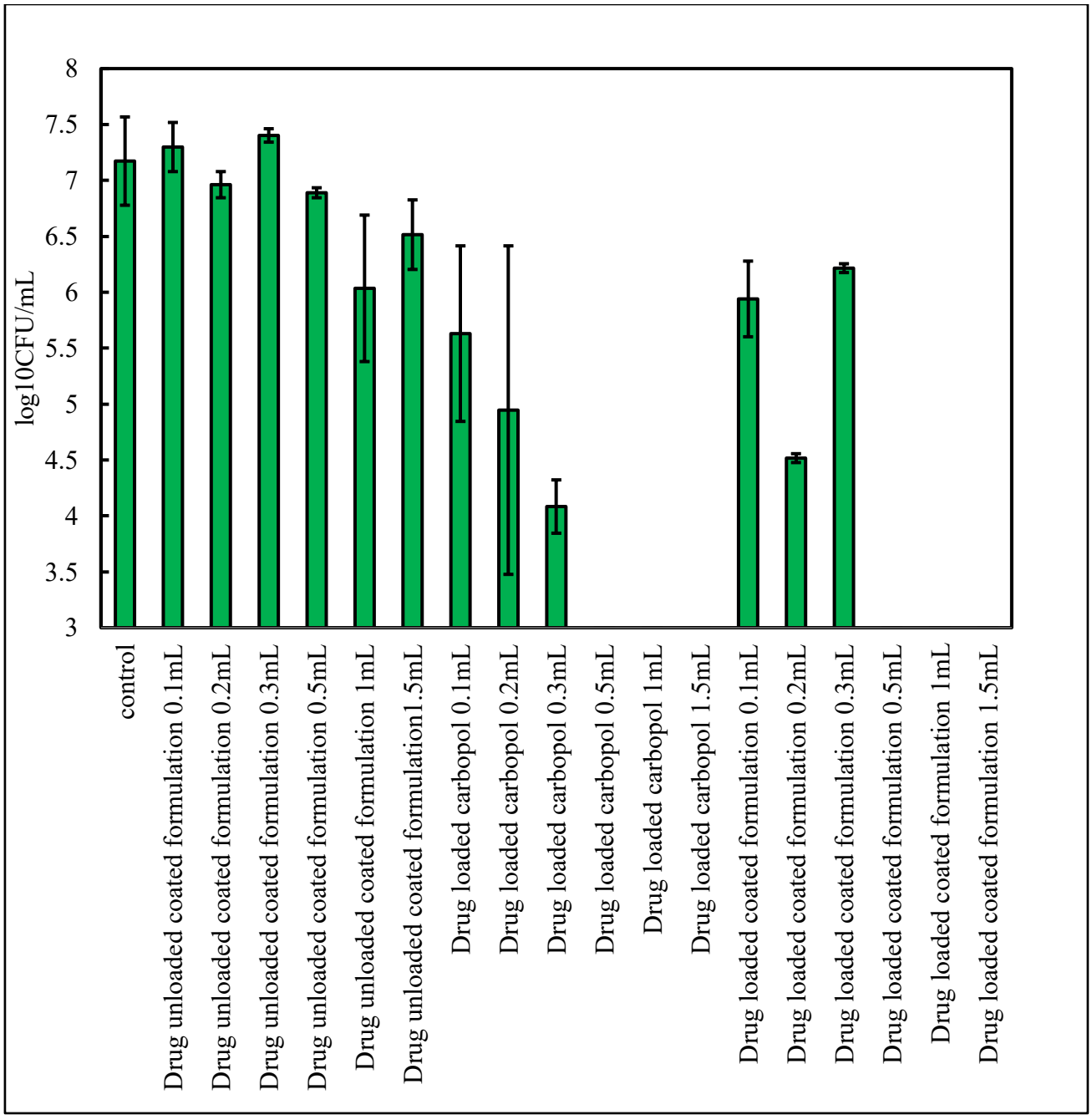

Figure 3.4. 2: CFU counts per mL of the PBS extract from the residual biofilm to account for the viable bacteria (S. epidermidis) following 24h of build up of a biofilm from bacterial broth in the presence of a variety of treatments at different aliquots of air-dried formulations compared with the control (no treatment).

Additionally, the same set of drug-loaded and unloaded coated formulations, as well as drug-loaded Carbopol formulations were mixed with bacterial broth and were evaluated using the CV assay. The control group, which did not undergo treatment, exhibited the highest residual biomass (100%) and used as a reference point for comparison. For the drug-unloaded formulations, a decrease in residual biomass was observed. However, no clear aliquot dependent trend was observed. The residual biomass values fluctuated between 54-65%. In contrast, the antibiotic loaded Carbopol formulations demonstrated a more significant decrease in biomass compared to the unloaded formulations. The greatest reduction in residual biomass was observed in the 1 mL formulation, which exhibited approximately 8.5% residual biomass. Similarly, the drug-loaded coated formulations showed a significant reduction in residual biomass. The antibiotic loaded BSA/shellac coated formulations demonstrated moderate decrease with the highest drug release observed in the 1.5 mL formulation. All results are shown in the Figure 3.4.3.

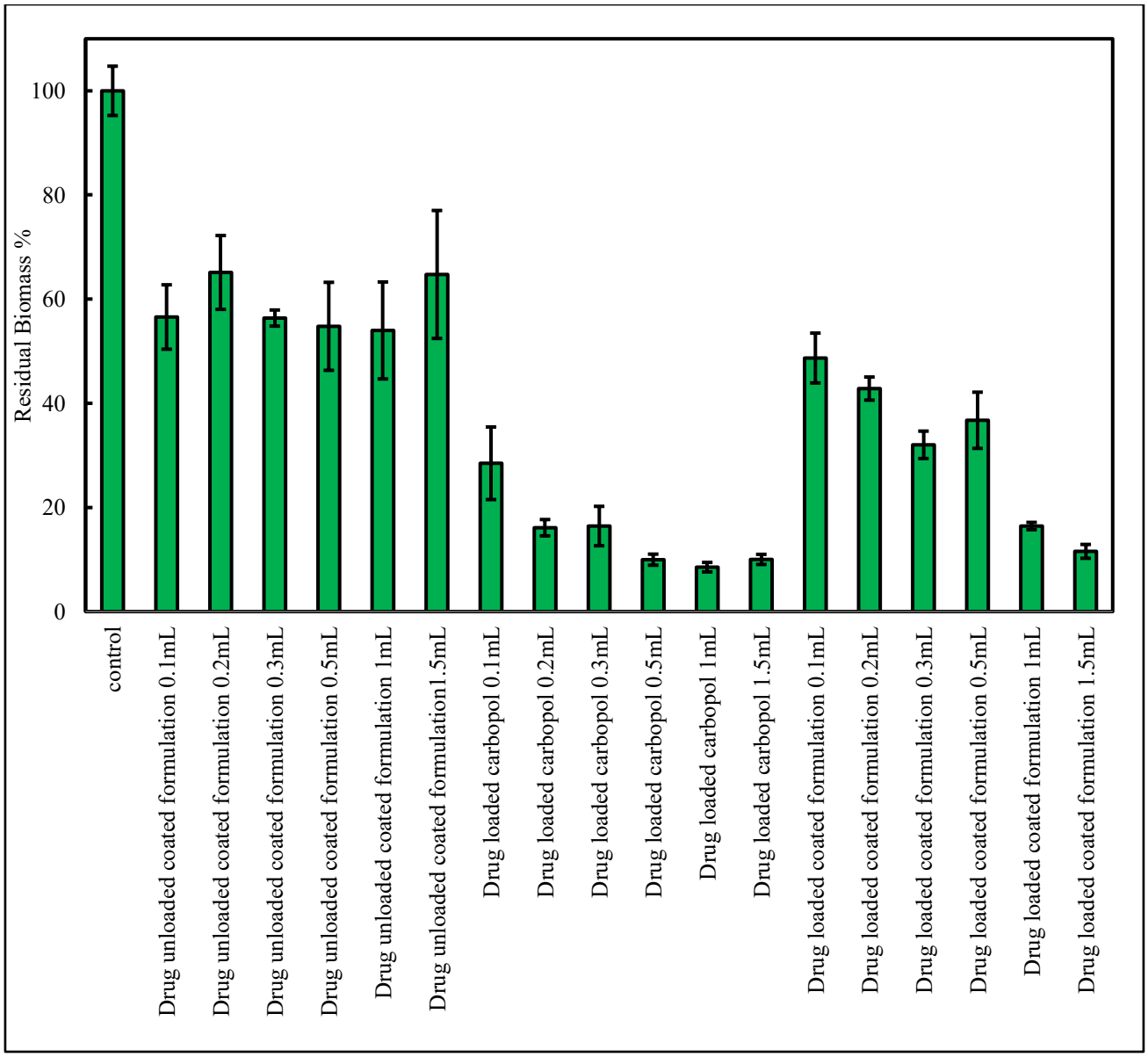

Figure 3.4. 3: Percentage of residual bacterial biofilm from S. epidermidis following 24h of growth under a variety of treatments with different aliquots non-loaded coated Carbopol, loaded non-coated Carbopol and loaded coated with BSA/shellac mixed with bacterial broth.

The effectiveness of both drug-loaded and unloaded formulations, mixed with bacterial broth, was assessed through a CFU count test, as shown in Figure 3.4.4. The control group, which did not receive any treatment, exhibited the highest CFU count per mL, indicating active bacterial growth. Drug-loaded Carbopol formulations and drug-loaded BSA/Shellac-coated particles demonstrated a significant reduction

in bacterial growth compared to the untreated control group. When comparing air-dried formulations to those mixed with bacterial broth, both sets showed a substantial reduction in CFU counts, with the most notable decrease observed in the antibiotic-loaded Carbopol and BSA/Shellac-coated formulations, particularly at volumes ranging from 0.5 to 1.5 mL. However, the 0.5 mL BSA/Shellac-coated formulation mixed with bacterial broth exhibited distinct results compared to its air-dried counterpart, suggesting potential differences in biofilm interaction or particle behavior under these conditions. Overall, the data indicate that drug-loaded formulations, especially at higher aliquot volumes, displayed the most effective antimicrobial activity.

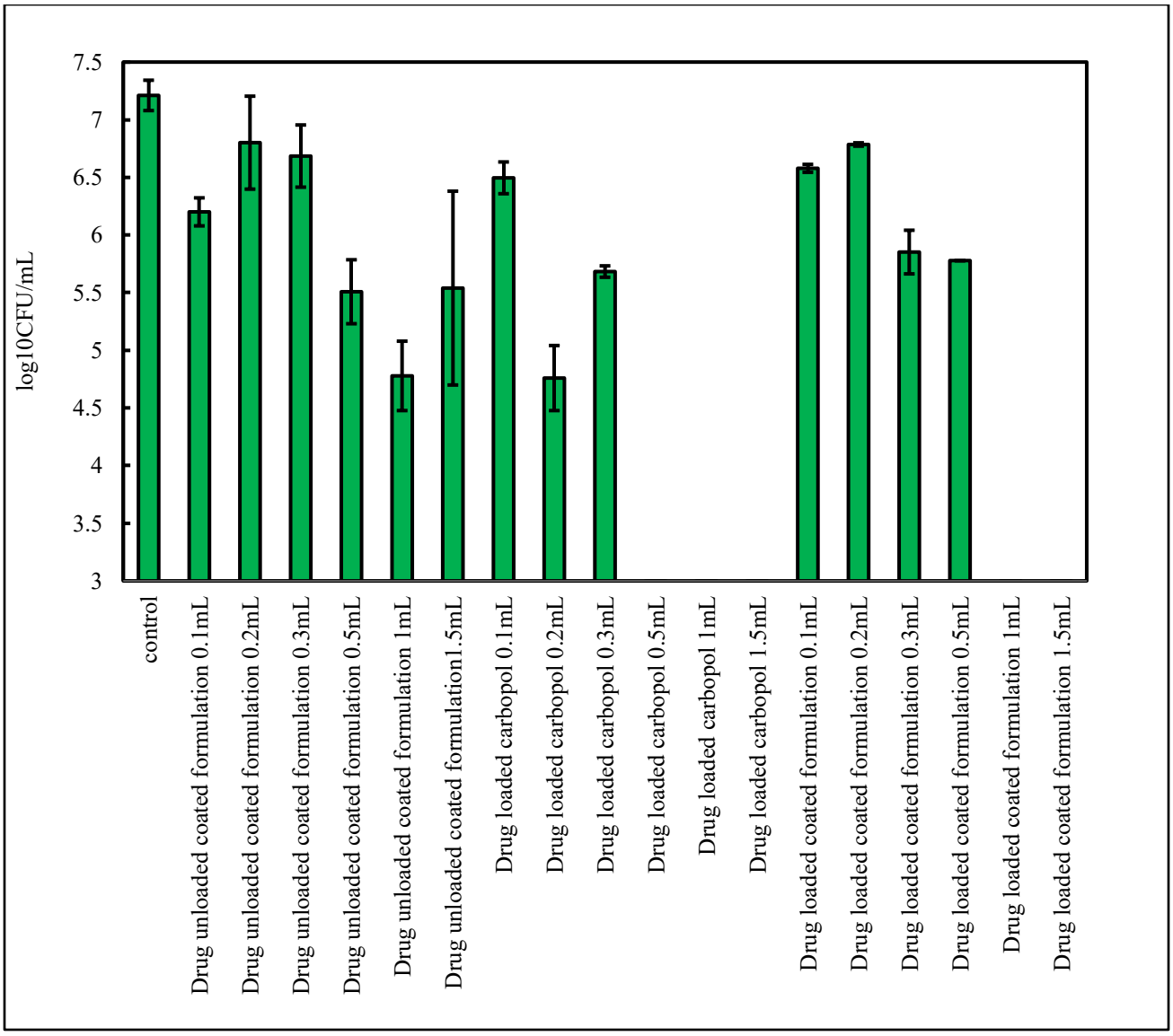

Figure 3.4. 4: CFU counts per mL of the PBS extract from the residual biofilm to account for the viable bacteria (S. epidermidis) following 24h of build up of a biofilm from bacterial broth in the presence of a variety of treatments at different aliquots and compared with the control (no treatment).

3.5 Cytotoxicity

MTS proliferation Assay

Figure 3.5.1 demonstrates how cell proliferation measurements were conducted by analyzing cell growth changes at different concentration levels of the formulations. Drug concentrations between 10 µL and 30 µL caused a concentration-dependent reduction in cellular growth, resulting in the lowest proliferation rate of 22.5% at the maximum concentration. When drug-loaded formulations were used at either 10 μL or 20 μL concentrations, they produced intermediate cellular results, reducing cell growth to 87.8% and 43.6%, respectively. The drug-unloaded formulations demonstrated better cell growth, especially at higher concentrations. Cell proliferation percentages for the unloaded formulations exceeded those of the drug-loaded formulations, reaching 116.6% at 10 μL, 91.6% at 20 μL, and 81.1% at 30 μL. Unloaded formulations showed less proliferative inhibition than their drug-loaded counterparts.

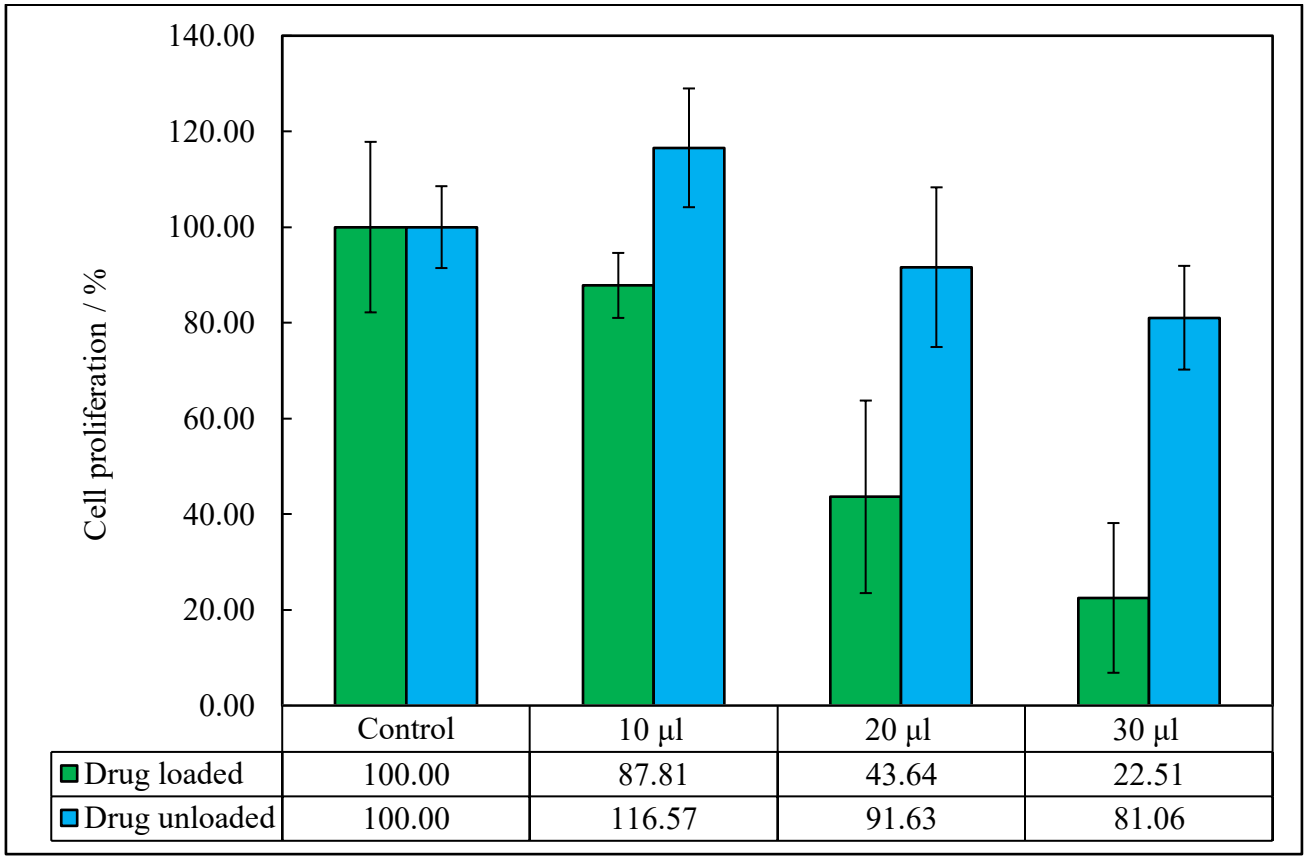

	Control	10 µl	20 µl	30 µl
Drug loaded	100.00	87.81	43.64	22.51
Drug unloaded	100.00	116.57	91.63	81.06

Figure 3.5. 1: Cell Proliferation of Drug-Loaded and Unloaded Formulations. Cell proliferation was assessed by measuring the percentage of cell growth following treatment with drug-loaded and drug-unloaded formulations at various concentrations (10 µL, 20 µL, and 30 µL)

The Hoechst/PI viability assay

Data in Figure 3.5.2 demonstrates that drug-loaded and drug-unloaded formulations had no major influence on cell viability, as tested concentrations from 10 µL to 30 µL maintained near 100% viability, with values of 98.7% and 94.2%, respectively. Assessment of cell viability between the control group at 89.9% and the highest concentration of 30 µL resulted in low variation, with a value of 78.3%. Drug-loaded formulations slightly reduced cell viability when administered at high concentrations, yet all values remained within the identified cytotoxicity limits.

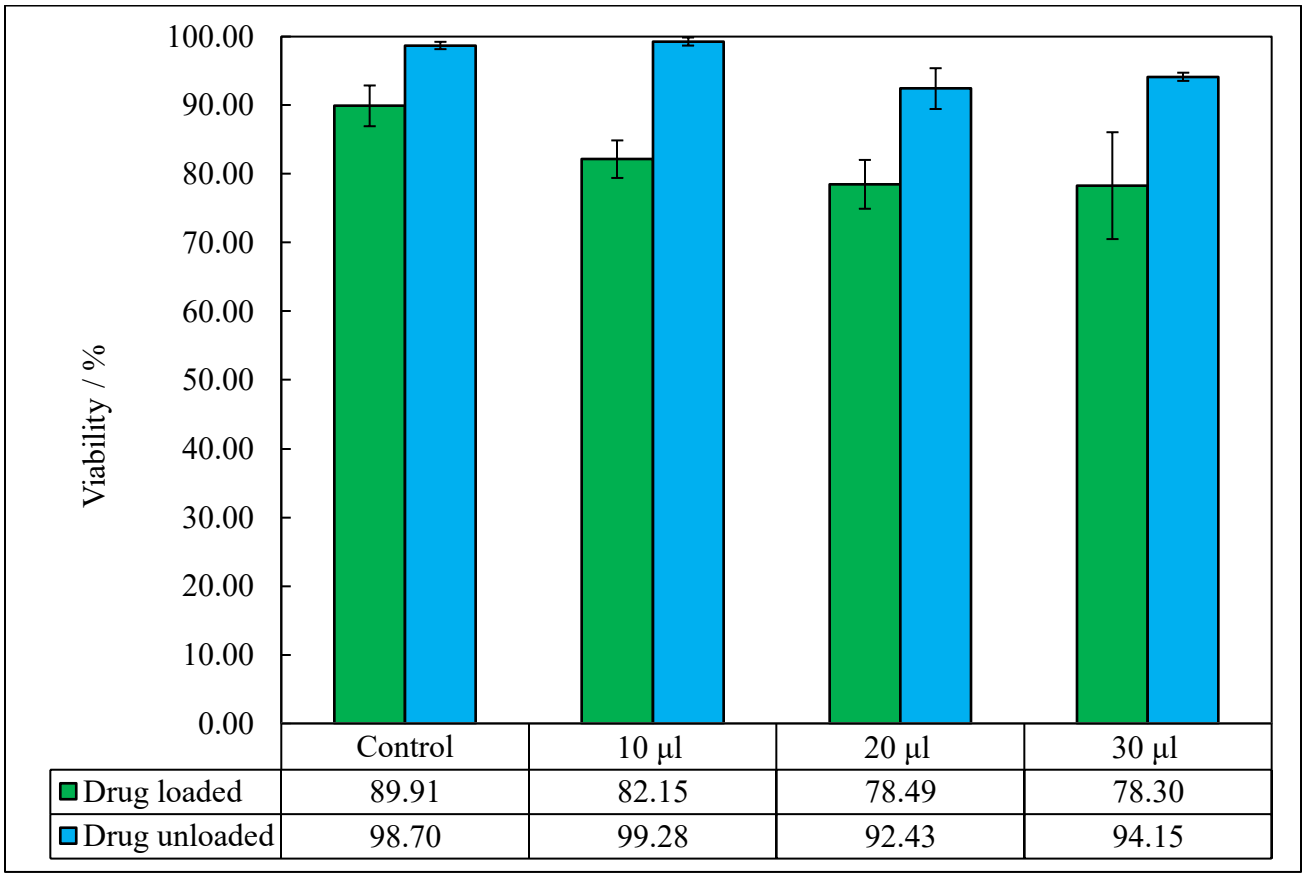

	Control	10 µl	20 µl	30 µl
Drug loaded	89.91	82.15	78.49	78.30
Drug unloaded	98.70	99.28	92.43	94.15

Figure 3.5. 2: Cell Viability of Drug-Loaded and Unloaded Formulations. Cell viability was measured using the viability assay for drug-loaded and drug-unloaded formulations at different concentrations (10 µL, 20 µL, and 30 µL)

The cell proliferation and viability test results on HaCaT cells reflect that drug-containing formulations deliver effective cell proliferation inhibition, reaching its highest point at 30 µL, leading to a 21.7% reduction in cellular proliferation over the course of 24h. Cell viability remained mostly consistent throughout all tested conditions, with the highest concentration of 30 µL showing slight reductions in viability. Cell proliferation assays showed no major inhibition effects from drug-unloaded formulations, as they sustained high cell viability across all analyzed nano-formulation concentrations. These findings suggest that the drug-loaded formulations possess effective anti-proliferative activity without significantly

compromising cell viability, indicating potential for therapeutic applications with minimal cytotoxicity.

Chapter 4

Conclusion

The research thesis describes a fully developed biologically triggerable nano-formulation systems that effectively protect against the formation of *Staphylococcus epidermidis* biofilm. The nano-formulation consists of an internal Carbopol nanogel core containing tetracycline hydrochloride, followed by BSA and Shellac coatings for enzyme-responsive and controlled release.

The nano-formulation achieved an encapsulation efficiency of 83.1% ± 0.64%, demonstrating high drug loading. The hydrodynamic diameter measurements increased from 126 ± 3.1 nm for drug-loaded Carbopol to 134 ± 5.0 nm for BSA-coated, and 153 ± 6.7 nm for BSA–Shellac-coated particles, indicating successful coating deposition. The zeta potential measurements showed a shift from –30 ± 0.5 mV for Carbopol to +31 ± 0.8 mV for BSA-coated particles and +26 ± 1.4 mV for BSA–Shellac-coated particles. These results indicate successful surface modification.

In vitro drug release studies demonstrated the system's responsiveness to enzymes. Drug release reached a maximum of 6 μg/mL over 41 hours in the absence of enzymes. Trypsin activation enabled a release of 10.2 μg/mL, closely approaching levels observed in uncoated drug-loaded Carbopol. These data confirm that bacterial proteases can trigger localized drug delivery.

The nano-formulation demonstrated its effectiveness through biofilm experiments, which revealed that optimal drug-containing coated system reduced biofilm biomass to 15% of original levels when used at a 1.5 mL volume. The CFU count experiment also showed antibacterial effects (i.e. the remaining viable bacteria in the biofilm) at higher quantities of drug-containing formulations.

Evaluation of nano-formulations cytotoxicity on HaCaT cell showed promising results, with cell viability remaining above 94% at lower doses and still reaching 78% at the maximum tested volume (30 µL per well).

Future work should focus on optimizing the nano-formulation concentration for clinical applications. Also, optimization of coating process, particularly the ratio of BSA and shellac, could enhance drug release profiles. However, most importantly identify volume and conventions of tetracycline-loaded BSA/shellac-coated Carbopol system that will release enough antibiotic to inhibit bacterial growth and insufficient to achieve full bactericidal action.

Bibliography

[1] P. Gupta, S. Sarkar, B. Das, S. Bhattacharjee, and P. Tribedi, “Biofilm, patho- genesis and prevention—a journey to break the wall: A review,” *Archives of Microbiology*, vol. 198, no. 1, pp. 1–15, Sep. 2015. doi: 10.1007/s00203-015-1148-6. [Online]. Available: https://doi.org/10.1007/s00203-015-1148-6.

[2] P. Di Martino, “Extracellular polymeric substances, a key element in understanding biofilm phenotype,” *AIMS Microbiology*, vol. 4, no. 2, pp. 274–288, Jan. 2018. doi: 10.3934/microbiol.2018.2.274. [Online]. Available: https: // pmc.ncbi.nlm.nih.gov/articles/PMC6604936/

[3] E. O. Asare, A. Seidakhanova, D. Amangeldinova, E. Marsili, and V. N. Paunov, “Targeting s. epidermidis biofilms by the tetracycline-loaded nanogel surface functionalized with savinase, dnase, and cellulase,” *ACS Applied Nano Materials*, vol. 6, no. 24, pp. 22 792–22 806, Dec. 2023. doi: 10.1021/acsanm.3c05410. [Online]. Available: https://doi.org/10.1021/acsanm.3c05410.

[4] H. Y. Liu, E. L. Prentice, and M. A. Webber, “Mechanisms of antimicrobial resistance in biofilms,” *Npj Antimicrobials and Resistance*, vol. 2, no. 1, Oct. 2024. doi: 10.1038/s44259-024-00046-3. [Online]. Available: https://www. nature.com/articles/s44259-024-00046-3.

[5] J. S. Ramírez-Larrota and U. Eckhard, “An introduction to bacterial biofilms and their proteases, and their roles in host infection and immune evasion,” *Biomolecules*, vol. 12, no. 2, p. 306, Feb. 2022. doi: 10.3390/biom12020306. [Online]. Available: https://doi.org/10.3390/biom12020306.

[6] A. Zhao, J. Sun, and Y. Liu, “Understanding bacterial biofilms: From definition to treatment strategies,” *Frontiers in Cellular and Infection Microbiology*, vol. 13, Apr. 2023. doi: 10.3389/fcimb.2023.1137947. [Online]. Available: https://doi.org/10.3389/fcimb.2023.1137947.

[7] D. Sharma, L. Misba, and A. U. Khan, “Antibiotics versus biofilm: An emerging battleground in microbial communities,” *Antimicrobial Resistance and Infection Control*, vol. 8, no. 1, May 2019. doi: 10.1186/s13756-019-0533-3. [Online]. Available: https://doi.org/10.1186/s13756-019-0533-3.

[8] E. O. Asare, E. A. Mun, E. Marsili, and V. N. Paunov, “Nanotechnologies for control of pathogenic microbial biofilms,” *Journal of Materials Chemistry B*, vol. 10, no. 27, pp. 5129–5153, Jan. 2022. doi: 10.1039/d2tb00233g. [Online]. Available: https://doi.org/10.1039/d2tb00233g.

[9] R. Mirzaei, R. Mohammadzadeh, M. Y. Alikhani, *et al.*, “The biofilm-associated bacterial infections unrelated to indwelling devices,” *IUBMB Life*, vol. 72, no. 7, pp. 1271–1285, Mar. 2020. doi: 10.1002/iub.2266. [Online]. Available: https:// doi.org/10.1002/iub.2266.

[10] A. Mishra, A. Aggarwal, and F. Khan, “Medical device-associated infections caused by biofilm-forming microbial pathogens and controlling strategies,” *An- tibiotics*, vol. 13, no. 7, p. 623, Jul. 2024. doi: 10.3390/antibiotics13070623. [Online]. Available: https://pmc.ncbi.nlm.nih.gov/articles/PMC11274200/ #sec2-antibiotics-13-00623.

[11] K. D. Mandakhalikar, J. N. Rahmat, E. Chiong, K. G. Neoh, L. Shen, and

P. A. Tambyah, “Extraction and quantification of biofilm bacteria: Method optimized for urinary catheters,” *Scientific Reports*, vol. 8, no. 1, May 2018. doi: 10. 1038 / s41598 - 018 - 26342 - 3. [Online]. Available: https :/ / www.nature.com/articles/s41598-018-26342-3.

[12] O. Diaconu, I. Siriopol, L. I. Polos, anu, and I. Grigoras, , “Endotracheal tube biofilm and its

impact on the pathogenesis of ventilator-associated pneumonia," *the Journal of Critical Care Medicine*, vol. 4, no. 2, pp. 50–55, Apr. 2018. doi: 10.2478/jccm-2018-0011. [Online]. Available: https://pmc.ncbi.nlm.nih. gov/articles/PMC6294989/.

[13] K. Moore, N. Gupta, T. T. Gupta, *et al.*, "Mapping bacterial biofilm on features of orthopedic implants in vitro," *Microorganisms*, vol. 10, no. 3, p. 586, Mar. 2022. doi: 10. 3390 / microorganisms10030586. [Online]. Available: https: //www.mdpi.com/2076-2607/10/3/586.

[14] S. Percival and P. Kite, "Intravascular catheters and biofilm control," *The Journal of Vascular Access*, vol. 8, no. 2, pp. 69–80, Apr. 2007. doi: 10． 1177/112972980700800202. [Online]. Available: https://doi.org/10.1177/ 112972980700800202.

[15] A.-A. Boisvert, M. P. Cheng, D. C. Sheppard, and D. Nguyen, "Microbial biofilms in pulmonary and critical care diseases," *Annals of the American Tho- racic Society*, vol. 13, no. 9, pp. 1615–1623, Jun. 2016. doi: 10.1513/annalsats. 201603 - 194fr. [Online]. Available: https : / / pmc . ncbi . nlm . nih . gov / articles/PMC5059503/.

[16] S. Dieckow, S. P. Szafrański, J. Grischke, *et al.*, "Structure and composition of early biofilms formed on dental implants are complex, diverse, subject-specific and dynamic," *Npj Biofilms and Microbiomes*, vol. 10, no. 1, Dec. 2024. doi: 10.1038/s41522- 024- 00624- 3. [Online]. Available: https://www.nature. com/articles/s41522-024-00624-3.

[17] A. Voinescu, M. Licker, D. Muntean, *et al.*, "A comprehensive review of micro- bial biofilms on contact lenses: Challenges and solutions," *Infection and Drug Resistance*, vol. Volume 17, pp. 2659–2671, Jun. 2024. doi: 10． 2147 / idr. s463779. [Online]. Available: https://pmc.ncbi.nlm.nih.gov/articles/ PMC11214797/.

[18] H. Y. Liu, E. L. Prentice, and M. A. Webber, "Mechanisms of antimicrobial resistance in biofilms," *Npj Antimicrobials and Resistance*, vol. 2, no. 1, Oct. 2024. doi: 10.1038/s44259-024-

00046-3. [Online]. Available: https://www. nature.com/articles/s44259-024-00046-3.

[19] H. Wu, C. Moser, H.-Z. Wang, N. Høiby, and Z.-J. Song, "Strategies for combating bacterial biofilm infections," *International Journal of Oral Science*, vol. 7, no. 1, pp. 1–7, Dec. 2014. doi: 10.1038/ijos.2014.65. [Online]. Available: https://www.nature.com/articles/ijos201465.

[20] C. Sahli, S. E. Moya, J. S. Lomas, C. Gravier-Pelletier, R. Briandet, and M. Hémadi, "Recent advances in nanotechnology for eradicating bacterial biofilm," *Theranostics*, vol. 12, no. 5, pp. 2383–2405, Jan. 2022. doi: 10.7150/thno. 67296. [Online]. Available: https:/ / pmc . ncbi. nlm . nihgov / articles/ PMC8899562/.

[21] R. Kun, M. Szekeres, and I. Dékány, "Isothermal titration calorimetric studies of the ph induced conformational changes of bovine serum albumin," *Journal of Thermal Analysis and Calorimetry*, vol. 96, no. 3, pp. 1009–1017, Jun. 2009. doi: 10.1007/s10973-009-0040-5. [Online]. Available: https://doi.org/ 10.1007/s10973-009-0040-5.

[22] M. K. Trivedi, "Spectroscopic characterization of chloramphenicol and tetracycline: An impact of biofield treatment," *Pharmaceutica Analytica Acta*, vol. 06, no. 07, Jan. 2015. doi: 10 . 4172 / 2153 - 2435 . 1000395. [Online]. Available: https://doi.org/10.4172/2153-2435.1000395.

[23] T. F. M. Oudemans, J. J. Boon, and R. E. Botto, "Ftir and solid-state13c cp/mas nmr spectroscopy of charred and non-charred solid organic residues pre- served in roman iron age vessels from the netherlands*," *Archaeometry*, vol. 49, no. 3, pp. 571–294, Aug. 2007. doi: 10.1111/j.1475-4754.2007.00321.x.[Online]. Available: https://doi.org/10.1111/j.1475-4754.2007.00321.x.

[24] Y. Chen, Z. Zhu, K. Shi, *et al.*, "Shellac-based materials: Structures, properties, and applications," *International Journal of Biological Macromolecules*, vol. 279,
p. 135 102, Aug. 2024. doi: 10 . 1016 / j. ijbiomac. 2024 . 135102. [Online]. Available: https://doi.org/10.1016/j.ijbiomac.2024.135102.

[25] A. S. Tsigara, C. N. Banti, A. Hatzidimitriou, and S. K. Hadjikakou, “Tetra-cycline: Structural characterization and antimicrobial properties of its water-soluble di-anionic bi-sodium salt,” Dalton Transactions, vol. 53, no. 29, pp. 12 080–12 089, Jan. 2024. doi: 10.1039/d4dt01384k. [Online]. Available: https://pubs.rsc.org/en/content/articlehtml/2024/dt/d4dt01384k.